Provided for non-commercial research and education use.
Not for reproduction, distribution or commercial use.

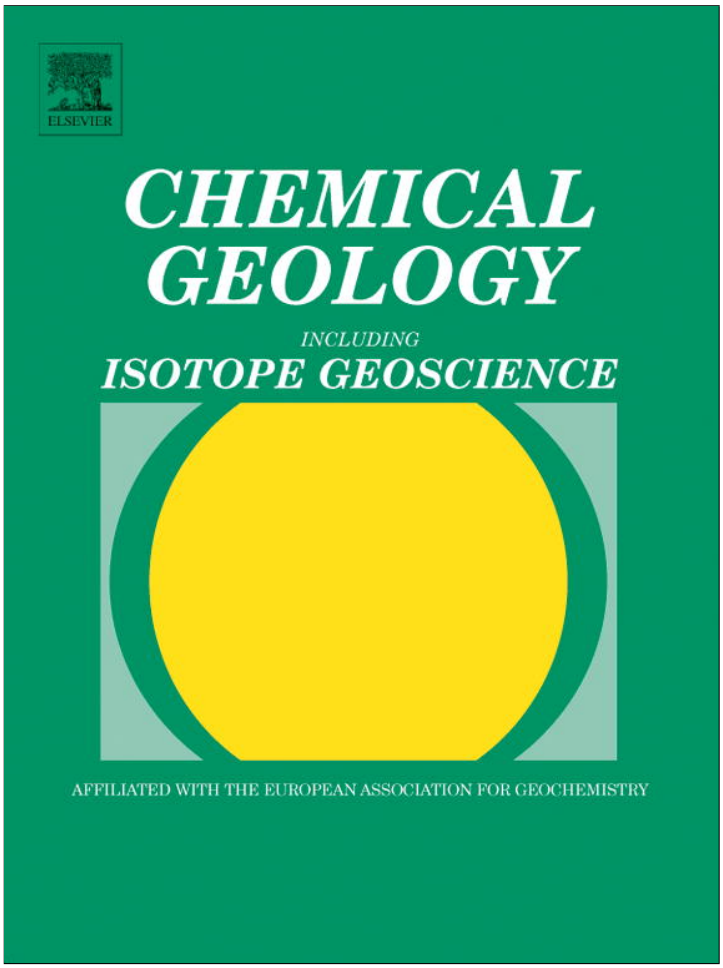

(This is a sample cover image for this issue. The actual cover is not yet available at this time.)

This article appeared in a journal published by Elsevier. The attached copy is furnished to the author for internal non-commercial research and education use, including for instruction at the authors institution and sharing with colleagues.

Other uses, including reproduction and distribution, or selling or licensing copies, or posting to personal, institutional or third party websites are prohibited.

In most cases authors are permitted to post their version of the article (e.g. in Word or Tex form) to their personal website or institutional repository. Authors requiring further information regarding Elsevier's archiving and manuscript policies are encouraged to visit:

http://www.elsevier.com/copyright

Author's personal copy

Chemical Geology 322–323 (2012) 121–144

Contents lists available at SciVerse ScienceDirect

Chemical Geology

journal homepage: www.elsevier.com/locate/chemgeo

The end-Permian mass extinction: A rapid volcanic CO_2 and CH_4-climatic catastrophe

Uwe Brand [a,*], Renato Posenato [b], Rosemarie Came [c], Hagit Affek [d], Lucia Angiolini [e], Karem Azmy [f], Enzo Farabegoli [g]

[a] Department of Earth Sciences, Brock University, St. Catharines, Ontario, Canada, L2S 3A1
[b] Dipartimento di Scienze della Terra, Università di Ferrara, Polo Scientifico-tecnologico, Via Saragat 1, 44100 Ferrara Italy
[c] Department of Earth Sciences, The University of New Hampshire, Durham, NH 03824 USA
[d] Department of Geology and Geophysics, Yale University, New Haven, CT 06520–8109 USA
[e] Dipartimento di Scienze della Terra, Via Mangiagalli 34, Università di Milano, 20133 Milan Italy
[f] Department of Earth Sciences, Memorial University, St. John's, Canada, NL A1B 3X5
[g] Dipartimento di Scienze della Terra e Geologico, Ambientali, Università di Bologna, Via Zamboni 67, 40126 Bologna, Italy

ARTICLE INFO

Article history:
Received 5 January 2012
Received in revised form 5 June 2012
Accepted 23 June 2012
Available online 2 July 2012

Editor: B. Sherwood Lollar

Keywords:
End-Permian mass extinction
Primary bLMC geochemistry—strontium, oxygen, carbon and clumped isotopes, REE
Extreme seawater temperatures
Continental erosion

ABSTRACT

The end of the Permian was a time of crisis that culminated in the Earth's greatest mass extinction. There is much speculation as to the cause for this catastrophe. Here we provide a full suite of high-resolution and coeval geochemical results (trace and rare earth elements, carbon, oxygen, strontium and clumped isotopes) reflecting ambient seawater chemistry and water quality parameters leading up to the end-Permian crisis. Preserved brachiopod low-Mg calcite-based seawater chemistry, supplemented by data from various localities, documents a sequence of interrelated primary events such as coeval flows of Siberian Trap continental flood basalts and emission of carbon dioxide leading to warm and extreme Greenhouse conditions with sea surface temperatures (SST) of ~36 °C for the Late Permian. Although anoxia has been advanced as a cause for the mass extinction, most biotic and geochemical evidence suggest that it was briefly relevant during the early phase of the event and only in areas of upwelling, but not a general cause. Instead, we suggest that renewed and increased end-Permian Siberian Trap volcanic activity, about 2000 years prior to the extinction event, released massive amounts of carbon dioxide and coupled with thermogenic methane emissions triggered extreme global warming and increased continental weathering. Eventually, these rapidly discharged greenhouse gas emissions, less than 1000 years before the event, ushered in a global Hothouse period leading to extreme tropical SSTs of ~39 °C and higher. Based on these sea surface temperatures, atmospheric CO_2 concentrations were about 1400 ppmv and 3000 ppmv for the Late and end-Permian, respectively. Leading up to the mass extinction, there was a brief interruption of the global warming trend when SST dropped, concurrent with a slight, but significant recovery in biodiversity in the western Tethys. It is possible that emission of volcanic sulfate aerosols resulted in brief cooling just after the onset of intensified warming during the end of the Permian. After aerosol deposition, global warming resumed and the biotic decline proceeded, and was accompanied by suboxia, in places of the surface ocean which culminated in the greatest mass extinction in Earth history.

© 2012 Elsevier B.V. All rights reserved.

1. Introduction

The end of the Permian witnessed the largest mass extinction of marine and non-marine biota in the Earth's geologic history. Approximately 90% of marine species, 70% of terrestrial vertebrate species (Maxwell, 1992; Jin et al., 2000; Ward et al., 2005), 30% of insect orders (Labandeira and Sepkoski, 1993) and an indeterminate percentage of terrestrial and marine plants disappeared during this catastrophe (Raup, 1979; Retallack, 1995; Kozur and Weems, 2011). This mass extinction was critical in laying the foundation for the rise and evolution of Mesozoic/Cenozoic marine and terrestrial life forms (Erwin, 1994). Numerous trigger and kill mechanisms have been proposed over the last few decades based on studies of rock sequences bracketing this mass extinction. Terrestrial perturbations, at the moment, appear to be favored over extraterrestrial causes (e.g., Retallack et al., 1998; Koeberl et al., 2010), but great uncertainty still surrounds the exact nature and process of the extinction (e.g., Erwin, 1994; Jin et al., 2000; White, 2002; Racki and Wignall, 2005; Knoll et al., 2007), as well as the duration and extent of the event (e.g., White, 2002; Brayard et al., 2011; Retallack et al., 2011; Shen et al., 2011a).

Studies have proposed a sudden, a step-wise or a gradual catastrophic end-Permian mass extinction (e.g., Magaritz et al., 1988; Holser et al., 1989; Jin et al., 2000). Some of the triggers put forward over the decades include: 1) bolide impact, 2) volcanism, 3) ocean anoxia, 4) seafloor methane, and 5) thermogenic methane emissions (e.g., Erwin, 1994; Racki and Wignall, 2005; Retallack and Jahren, 2008). These may bring into play synergistic or antagonistic kill

* Corresponding author.
E-mail address: uwe.brand@brocku.ca (U. Brand).

0009-2541/$ – see front matter © 2012 Elsevier B.V. All rights reserved.
doi:10.1016/j.chemgeo.2012.06.015

Author's personal copy

mechanisms such as: 1) niche (habitat) loss, 2) hypercapnia, 3) global cooling, 4) hyposalinity, 5) global warming—CO_2, 6) global warming—CH_4, 7) low atmospheric oxygen, 8) global depletion of stratospheric ozone, 9) ocean acidification, 10) nutrient limitation (shutdown of terrestrial and marine productivity), 11) acid rain, 12) poisoning from toxic gases, and other related mechanisms such as 13) biosphere upheaval through forced migration and increased competition, 14) extraordinary spread and transmission of disease, and 15) life cycle disruption(s) due to increased environmental stresses (e.g., Erwin, 1994; Kidder and Worsley, 2004; Racki and Wignall, 2005; Knoll et al., 2007; Wignall, 2007; Grasby et al., 2011). These postulated mechanisms might have acted alone or in concert, with many researchers favoring a tangled web of interactions and related causes and effects (e.g., Erwin, 1994; Knoll et al., 2007; Wignall, 2007). Recent advances in the study of the end-Permian mass extinction suggest, 1) close association in time between the marine and terrestrial extinctions (e.g., Sephton et al., 2002; Kidder and Worsley, 2004; Shen et al., 2011a), 2) rapid onset of this catastrophe (revised down from 165,000 to 20,000 years; Bowring et al., 1998; Rampino et al., 2002; Reichow et al., 2009; Shen et al., 2011a) and, 3) long duration (~5 Ma) for full biotic recovery during the early Triassic (e.g., Kozur, 1998; Benton et al., 2004; Korte and Kozur, 2010; Brayard et al., 2011). However, the latter two points, particularly the long recovery (cf. Payne et al., 2004) are intensely debated, and more detailed sedimentological, paleobiological, geochemical and stratigraphic studies are needed to resolve them. Modeling of the various causes has put forth Siberian flood basalt volcanism and oceanic anoxia as leading triggers ultimately responsible for this mass extinction (e.g., Smith, 1995; Wignall and Twitchett, 1996; Kamo et al., 2003; Benton et al., 2004; Kidder and Worsley, 2004; Racki and Wignall, 2005). But, despite the many advances in describing and characterizing the end-Permian interval, we still lack a definitive theory for a trigger and kill mechanism(s) for this massive life ending and changing event at the close of the Paleozoic.

Geochemical quantification of this event commenced with the analysis of whole rock $\delta^{13}C$ trends about the Permo-Triassic boundary (PTB) from China, Austria and Italy, as well as other localities of the Tethys (Fig. 1; Chen et al., 1984; Baud et al., 1989; Holser et al., 1989). These pioneering studies showed negative $\delta^{13}C$ excursions heralding the PTB and extinction event, and were followed by many other studies of sections from around the world covering this same interval (e.g., Racki and Wignall, 2005; Korte and Kozur, 2010). Despite uncertainties in the magnitude and duration of the recorded $\delta^{13}C$ excursions, as well as in their stratigraphic assignment and correlation, the global nature of the negative $\delta^{13}C_{carb}$ shift in the seawater-^{13}C curve preceding the event and/or PTB appears to be unequivocal (Korte and Kozur, 2010). Mind that no adjustment was ever made in these studies to the assumed primary $\delta^{13}C_{carb}$ values for differences in mineralogy of the original whole rock (e.g., Rubinson and Clayton, 1969), which may now be diagenetic low-Mg calcite (dLMC), dolomite or mixtures thereof (cf. Brand and Veizer, 1980). Such adjustment is critical, when comparing whole rock (assuming it was originally aragonite or a mixture of carbonate phases) to brachiopod low-Mg-calcite (bLMC) primary $\delta^{13}C$ values. Some studies have used other elements/isotopes as proxies of changes in the associated bio-, atmos-, lithos- and hydro-spheres with limited success (e.g., Dolenec et al., 2001; Gorjan et al., 2008). Others have used biogenic allochems as proxy material instead of whole rock (Gruszczynski et al., 1989; Martin and MacDougall, 1995; Korte et al., 2005; Kearsey et al., 2009) with some studies evaluating the mass extinction from an oceanic perspective (Musashi et al., 2001; Isozaki, 2009; Korte and Kozur, 2010).

In this study, we combine the geochemistry of whole rock and biogenic carbonates from several locations into an integrated set of high-resolution geochemical seawater curves for the end of the Permian. Low-Mg calcite of brachiopod shells is quite resistant to diagenetic alteration, and when preserved, may contain geochemical compositions of the ambient seawater (Brand and Veizer, 1980, 1981; Brand et al., 2003; Brand, 2004). In order to determine the cause for the end-Permian event, we examined brachiopods and whole rock at high stratigraphic resolution covering several meters at: Sass de Putia (N 46° 39′ 50″, E 11° 49′ 51″, elev. 2150 m) and Val Brutta (N 46° 00′ 06″, E 11° 26′ 12″, elev. 1076 m; Farabegoli et al., 2007; Posenato, 2009, 2010 and references therein) in northern Italy, with some additional material/information obtained from sections at Tesero (N 46° 17″ 14.34″, E 11° 30″ 53.83″) and Bulla (N 46° 34′ 12.87″, E 11° 37′ 46.27″; Fig. 2).

We first screened all studied material for diagenetic alterations, and, then we used only pristine material to construct a robust picture of environmental conditions using all available geochemical information from trace elements (Ca, Mg, Sr, Na, Mn and Fe), redox-sensitive elements (U, Th), rare earth elements (La, Ce, Pr, Nd), isotopes (C, O, Sr) and clumped isotopes (Δ_{47}) for the end of the Permian of northern Italy, and compared these new results to information available from other sections. Finally, we compared global seawater-^{87}Sr, -^{13}C, -^{18}O curves to changing biodiversity levels prior and during the end-Permian mass extinction, in order to reconstruct seawater parameters, such as changes in global SST, oceanic redox, continental weathering and pCO_2 levels for the end of the Permian.

2. Methods

Brachiopods and coeval whole rock were collected with high precision and resolution (at the cm level, measured relative to the Bellerophon–

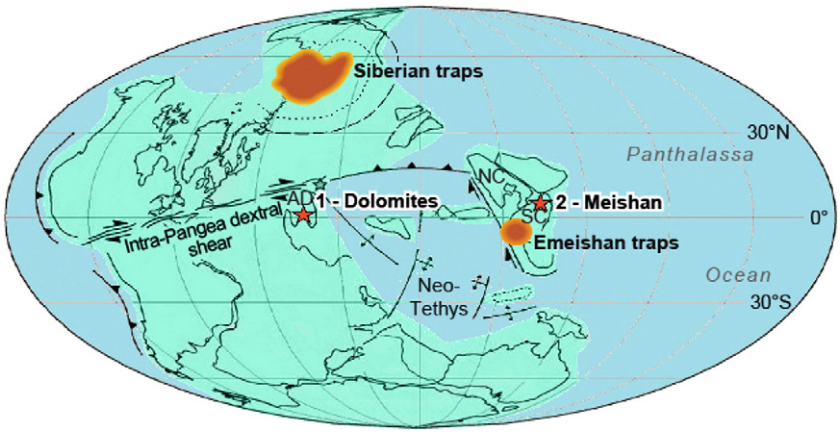

Fig. 1. Continental configuration of Pangaea during the late Permian with P/T boundary areas in northern Italy (1—Dolomites) and China (2—Meishan; modified after Muttoni et al., 2009). The Emeishan and Siberian Traps are included, and the uncertainty in the areal extent of the Siberian continental flood basalt province is denoted by the dashed lines (Dorritie, 2002; Racki and Wignall, 2005).

Author's personal copy

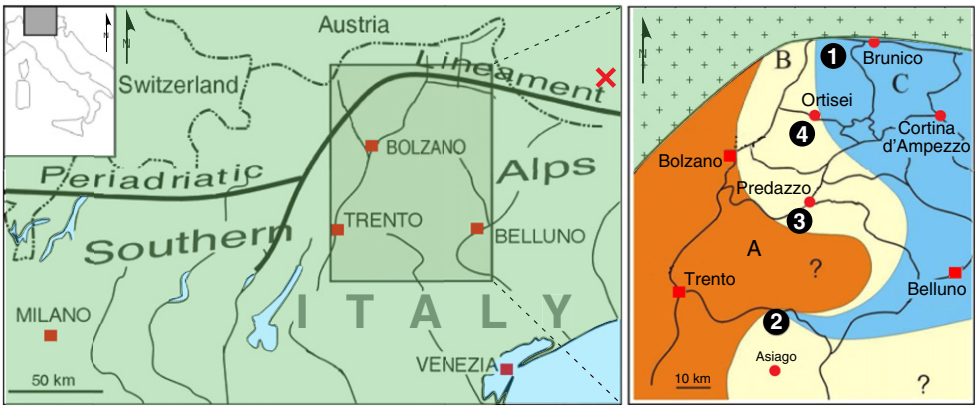

Fig. 2. Study sections in Northern Italy and the Southern Alps region of Trento and Bolzano. Section 1 is Sass de Putia, Section 2 is Val Brutta, Section 3 is Tesero and Section 4 is Bulla of northern Italy, at the western-most extremity of the Paleo-Tethys Sea (Posenato, 2009). Area 'A' represents terrestrial and near-shore environments, area 'B' represents restricted marine conditions, area 'C' represents a fully open marine environment, and 'X' denotes locality of the Gartnerkofel-1 core (Austria).

Werfen Formational boundary) from several end Permian sections in the Southern Alps. The detailed geochemical data are presented in Appendices 1 and 2.

2.1. Sample collection and preparation

A total of 132 samples (97 brachiopods, 32 whole rocks, and 3 cements) were collected from three carbonate successions representing the Bulla and Tesero Members of the end of the Permian in the eastern Southern Alps of northern Italy (Figs. 2 and 3). Brachiopods were physically separated from the enclosing whole rock, and both components were further cleaned by physical and chemical means, consisting of scraping and removing the outermost surface of brachiopod shell fragments and weathered rinds of the whole rock. Subsequently all separated materials were leached with 10% HCl to remove any remaining cross-contamination from surfaces, cracks and crevices. Samples were visually and optically inspected by transmitted light microscopy, cathodoluminescence and scanning electron microscopy prior to powdering and subsequent geochemical analysis. Covered and uncovered thin sections were cut for these procedures from rock fragments.

2.2. Analytical techniques

A subset of brachiopod fragments was retained for SEM analysis for screening of microstructural integrity. This work was carried out on an AMRAY 1600 scanning electron microscope at Brock University. Luminescence of uncovered rock thin sections (50 μm thick) was determined with a NUCLIDE ELM-2B cathode luminescope and operating conditions of 45 mTorr (vacuum), 0.6 mA (beam current), 11–15 KVA (voltage) and 6 s exposure time (normal). Other thin sections, cut 30 μm thick, were stained with Alizarin Red and potassium ferricyanide and examined by polarizing microscope (LEITZ) for standard petrographic parameters such as textural, microstructural and chemical indicators of diagenesis (qualitative Fe content; Lindholm and Finkelman, 1972).

2.2.1. Trace element analysis

About 10–30 mg of powder, weighed to four decimal places, of each sample was digested with 10 mL of distilled 2% (v/v) HNO_3. Modifiers (K and La solutions) were added to the solutions, where appropriate, to counter chemical interferences. High-Purity reference standards (Delta Scientific) were used to calibrate the atomic absorption spectrophotometer (AAS) for each element. All samples were analyzed on a VARIAN 400P AAS for Ca, Mg, Sr, Na, Mn and Fe at Brock University. Long-term precision and accuracy, based on the mean of 46 analyses of standard reference material (SRM) NBS 633, of analytical work was 4.79, 0.88 (Ca), 4.51, 0.93 (Mg), 6.61, 0.76 (Sr), 5.98, 2.49 (Na), 4.32, 2.11 (Mn) and 8.57, 3.35 (Fe) relative percent (±%), respectively, of certified SRM values.

2.2.2. REE analysis

Redox sensitive trace elements (Th and U) and REEs were analyzed at Memorial University. About 5 mg of powder of each sample was digested in 0.2 M HNO_3 for 70–80 min and analyzed by standard addition techniques for elements using a Perkin Elmer Sciex Elan DRCII ICP-MS. The relative uncertainties, accuracy and precision compared to SRM DLS 88a, of measurements are better than ±5% (Azmy et al., 2011). The weak acid leach used in this method only captures soluble elements associated with the carbonate fraction and leaves the non-carbonate materials essentially untouched and a non-contributory factor to the reported trace and REE chemistry of the sediments from northern Italy. For REE results, $(Ce/Ce^*)_{SN}$ values of >1 represent anoxic depositional conditions, whereas <1 represent oxic ones (e.g., Bau and Dulski, 1996; Azmy et al., 2011). Similarly, the conversion of U^{6+} into uranyl carbonate reflects oxic conditions with Th/U of >2, and corresponds to anoxic water conditions at Th/U of <2 (Wignall and Twitchett, 1996); but its application to carbonates is complicated (Klinkhammer and Palmer, 1991). Instead, Jones and Manning (1994) proposed other redox indices, which including authigenic U content of >12 ppm indicates suboxic and anoxic conditions, whereas a content of <5 ppm indicates oxic water conditions. Thus, we will use the Ce anomaly and authigenic U indices to characterize the depositional redox conditions of end of the Permian seawater and carbonates of the Southern Alps.

2.2.3. Carbon, oxygen and strontium isotope analyses

Samples were analyzed for carbon and oxygen isotopes at Memorial University. About 200 μg of powder of each sample was reacted with ultrapure 100% orthophosphatic acid at 50 °C in a Thermo-Finnigan Gasbench II, and liberated CO_2 gas was introduced into a Thermo-Finnigan Delta V mass spectrometer. Long-term precision and accuracy compared to NBS-19 standard values were better than 0.05‰ for both $\delta^{13}C$ and $\delta^{18}O$.

A subset of samples was analyzed for Sr isotopes at Ruhr University, Bochum. About 1 mg of each sample was digested with 2.5 N suprapure HCl for about 24 h at room temperature. This was followed by chromatographic separation with 2.5 mL of AGW 50×8 (Biorad) cation exchange resin to obtain purified Sr. Samples were prepared and analyzed on a Finnigan MAT 262 7-collector solid-source mass spectrometer with single Re filament applying 1 μL of ionization enhancing solution (Birck, 1986). Loading blank was below 5 pg, column blank was less than 1 ng, and reagent blank was below 0.01 ppb. The mean of 193 analyses of NIST standard NBS 987 was 0.710240 with a mean standard error of 0.000006 (±2σ) and mean standard deviation of

Author's personal copy

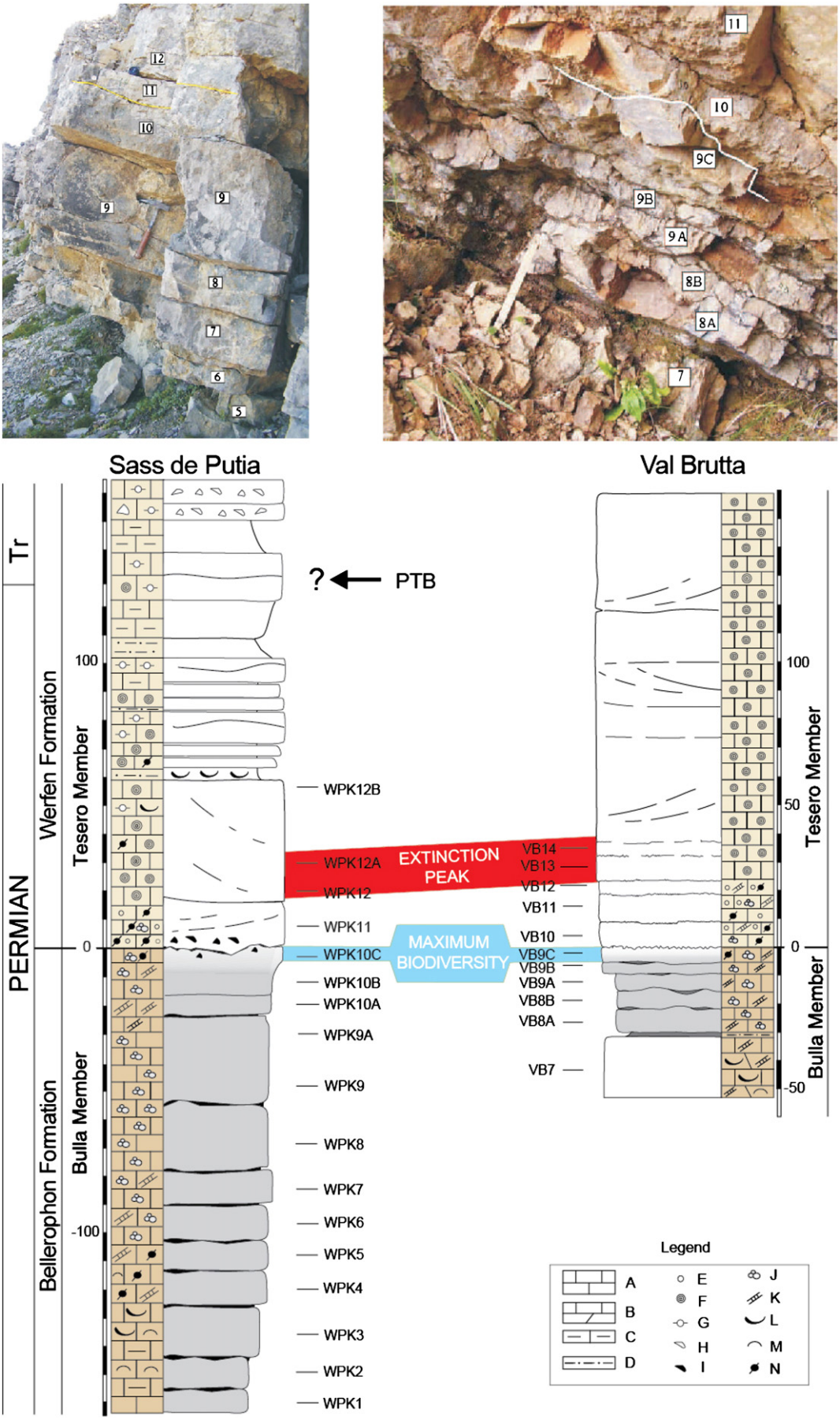

Author's personal copy

0.000036 (±2σ), whereas the mean of 182 analyses of the USGS EN-1 standard was 0.709159 with a mean standard error of 0.000004 (±2σ) and mean standard deviation of 0.000028 (±2σ). The strontium isotope values of this study were bracketed by and corrected to a nominal NBS-987 value of 0.710247 (McArthur et al., 2001).

2.2.4. Δ_{47} Analysis and standardization

Another subset of samples (the best-preserved after exhaustive diagenetic screening, see below) was analyzed for clumped isotope compositions at Yale University. These analyses involve simultaneous measurement of the ion beams corresponding to masses 44 to 49, with masses 44, 45, and 46 reflecting $\delta^{13}C$ and $\delta^{19}O$ values of CO_2 and mass 47 reflecting the clumped isotope signal. Masses 48 and 49 are used to screen for interferences due to organic contaminants in CO_2 samples (Eiler, 2007).

The clumped isotope technique yields paleotemperatures that are independent of the composition of the water from which the shell-carbonate precipitated (Ghosh et al., 2006). It is based on the mass-47 ion beam that includes contributions from three isotopologues: $^{18}O^{13}C^{16}O$, $^{17}O^{12}C^{18}O$ and $^{17}O^{13}C^{17}O$. This population is overwhelmingly dominated by $^{18}O^{13}C^{16}O$, and so largely reflects the abundance of $^{13}C-^{18}O$ bonds in reactant carbonate. Data are reported as Δ_{47}, defined as the deviation of R^{47} (the abundance ratio of mass 47 to mass 44 isotopologues) from that expected at 'stochastic distribution', namely when the abundance of isotopologues is determined by random distribution of the rare isotopes among all possible isotopologues, and following:

$$\Delta_{47} = \left[\frac{R^{47}}{2R^{13}\cdot R^{18} + 2R^{17}\cdot R^{18} + R^{13}\cdot\left(R^{17}\right)^2} - \frac{R^{46}}{2R^{18} + 2R^{13}\cdot R^{17} + \left(R^{17}\right)^2} - \frac{R^{45}}{R^{13} + 2R^{17}} + 1\right] \times 1000.$$

Carbonate (3–4 mg) was digested in an overnight reaction with 105% phosphoric acid at 25 °C. Resultant CO_2 was extracted from all samples using the laboratory methods described in Ghosh et al. (2006), which are an extension of well-established phosphoric-acid digestion methods (e.g., Swart et al., 1991). Product CO_2 was purified cryogenically on a vacuum line, and then passed through a GC column (Supelco Q Plot column, 30 m long, 530 μm ID) at −20 °C, and analyzed in a dual inlet Finnigan MAT 253 gas-source mass spectrometer. The mass spectrometer was configured to collect masses 44 through 49 and standardized by comparison with CO_2 gases of known isotopic composition that had been heated for 2 h at 1000 °C in order to achieve stochastic isotopic distribution (Δ_{47} = 0‰; Ghosh et al., 2006). Several heated gas standards, spanning a range of bulk stable isotope compositions, were analyzed in order to account for mass spectrometric nonlinearity (Huntington et al., 2009). Masses 48 and 49 were monitored to assure adequate sample purification. Each measurement consisted of 9 acquisitions of 10 cycles of sample-reference gas comparison each, with 20 s integration time, using a signal of 16 V in mass 44 (Huntington et al., 2009; Zaarur et al., 2011). Shot noise precision is typically 0.009‰ per run. Measurements were replicated 1–5 times (depending on material availability) for an average precision with standard deviations (between acquisitions) of 0.02‰ in Δ_{47} (resulting in general temperature uncertainty for the data set of ~±3 °C). Scale compression due to ion source chemistry and isotopic scrambling was accounted for by analyzing CO_2 equilibrated at several temperatures through isotope exchange with water and a set of laboratory work standards whose Δ_{47} value was defined through an interlaboratory comparison (Dennis et al., 2011). The data are reported using the same reference frame used in the original Δ_{47}–T calibration of Ghosh et al. (2006; Zaarur et al., 2011). In Appendix 2, we report the data using the both the traditional and newly defined absolute reference frame (Δ_{47abs}, Dennis et al., 2011).

As part of the Δ_{47} analyses, $\delta^{18}O$ and $\delta^{13}C$ were simultaneously acquired. The acquired Δ_{47} values were converted to carbonate growth temperature using the following relationship (Ghosh et al., 2006):

$$\Delta_{47} = 0.0592*\left(10^6*T^{-2}[K]\right) - 0.02. \quad (2)$$

Paired temperature and bLMC $\delta^{18}O$ data were used to calculate the $\delta^{18}O$ value of the water from which the carbonates grew using the following equation (based on the Kim and O'Neil, 1997 temperature-$\delta^{18}O$ calibration, corrected to 10.25 ‰ acid reaction fractionation; Came et al., 2007):

$$10^3 \ln_\alpha(c-sw) - 18.03*\left(10^3/T[K]\right) + 32.17 \quad (3)$$

In two bLMC samples uncertainty in clumped isotope results was observed that is far beyond the typical analytical uncertainty. These are bLMC samples from horizons wPK3 (−132 cm, Sass de Putia) and VB 10 (+9 cm, Val Brutta, Appendix 2). In the first instance (wPK3), the lower clumped isotope temperature result is due to an extremely small sample, which produced a marginal amount of CO_2 and because of the small size we were unable to repeat the analysis. Instead, we used a complementary sample from the same horizon (this analysis included replicates). Similarly, clumped isotope analyses of two separate bLMCs from horizon VB 10 give slightly inconsistent results. In this instance, the slightly higher seawater-^{18}O value is more in line with those that preceded this particular horizon, and similar results were obtained during the initial sample run for both samples. Thus, the later analyzed and slightly anomalous values are considered compromised by instrumental instability. Considering all factors (geological, biological and analytical) the slightly higher temperature and ^{18}O-enriched water compositions are deemed the most representative and 'natural' of end of the Permian seawater. Note, although only the best-preserved samples were selected for clumped isotope analysis, the highest temperatures may reflect a small degree of alteration due to atomic scale solid-state diffusion within calcite. This type of alteration has a unique effect on clumped isotopes, but is impossible to detect by the diagenetic indicators used in this study. For samples that are otherwise pristine, this effect may lead to a small increase in apparent temperature, depending, in part, on burial temperature and time (Eiler, 2011; Affek, 2012).

3. General geology and stratigraphy

The south-verging thrust belt area of the Southern Alps is separated from the northern part by the Periadriatic or Insubric Lineament (Fig. 1), and both represent an autochthonous part of the Apulia or Periadriatic Plate. The Permian succession of the Southern Alps consists of two major tectono-sedimentary cycles separated by a long hiatus (15–30 Ma) corresponding to the late Cisuralian and Guadalupian (Cassinis and Perotti, 2007). The transgressing sea and its incumbent marine conditions reached the Adige Valley (Trento and Bolzano, Fig. 2) during the Late Permian (Assereto et al., 1973). Concurrently during this time, in the western Southern Alps (Lombardy) only continental sediments are present, whereas in the Dolomites and Carnia (east of the Adige Valley, eastern Southern Alps) the sedimentary succession, up to 1000 m thick in the depocentre, consists of red beds followed by evaporites and shallow marine carbonates of the Val

Fig. 3. Outcrops and stratigraphic columns at Sass de Putia (wPK) and Val Brutta (VB), northern Italy. The columns depict the sample horizons (wPK and VB, Appendix 1). Legend: A, limestone; B, dolomitized limestone; C, marly limestone; D, silty marl; E, crystalline ooid; F, ooid; G, oncoid; H, intraclast; I, reworked clast; J, foraminifera; K, calcareous alga; L, mollusc; M, ostracod; N, reworked microfossil.

Author's personal copy

Gardena Sandstone and Bellerophon Formation, respectively. The succession is punctuated by third-order transgressive regressive and/or tectono-sedimentary cycles, which depict complex vertical and lateral stratigraphic relationships (Farabegoli et al., 1986; Massari et al., 1994; Perri and Farabegoli, 2003).

Studied since the 19th century, the upper carbonates of the Bellerophon Formation yield rich and abundant marine fossil assemblages (see Posenato, 2010 for many references). Litho- and bio-facies consisting of wacke- and packstones imply a low gradient low-energy ramp within the photic zone (Massari and Neri, 1997). Precise dating of the Bellerophon Formation is difficult, because the restricted and/or very shallow marine environment limited settlement to fully stenotopic marine organisms. Ammonoids (*Paratirolites* sp.) and conodonts (*Hindeodus typicalis*) appear in the upper 50 m of the formation where they indicate a late Changhsingian age. Conodonts are abundant in the overlying Werfen Formation facilitating recognition of the Permo-Triassic boundary and Induan biozones (Fig. 3; Perri and Farabegoli, 2003).

3.1. Stratigraphy of the Bellerophon–Werfen Formational Boundary

The upper Bellerophon Formation, a 10–25 m regionally regressive ostracod and peritidal dolomite unit, contains indisputable evidence (mud cracks and vertical roots) of emergence (Broglio Loriga et al., 1988; Farabegoli et al., 2007). The uppermost 1.40 m of the formation comprises the Bulla Member (Perri and Farabegoli, 2003; Farabegoli et al., 2007), which is predominantly a dark grey to black fossiliferous wacke-/packstone (Fig. 3). In the uppermost Bulla Member, foraminifera and brachiopod biodiversity reach their maximum for the formation (Table 1; Broglio Loriga et al., 1988; Posenato, 2001, 2010). Brachiopods in the upper beds are represented by *Comelicania*, *Comelicothyris*, *Janiceps*, *Ombonia*, *Orthothetina*, and *Septospirigerella*?, whereas *Comelicania* dominate the underlying beds (Posenato, 2001, 2010).

Conodonts are only known in the eastern Dolomites at the Ansiei section, characterizing the latest Changhsingian *Hindeodus praeparvus* Zone (Perri and Farabegoli, 2003; Farabegoli et al., 2007). On the basis of conodont zonation and depositional characteristics (Fig. 4A, B), the Bulla Member is correlated with Bed 24e of the GSSP at Meishan (Yin et al., 2001; Horacek et al., 2010; Posenato, 2010), which is located immediately below the end – Permian mass extinction event.

The skeletal limestone of the Bulla Member, separated by an erosional surface, is overlain by ooid grainstone of the Tesero Member (Werfen Formation, Fig. 4C–E). Reworked foraminifera and geopetal, oxidized matrix from the regressive Bulla and transgressive Tesero grainstones, suggest a rapid sea level drop, emersion and erosion of more elevated areas. The low topographic relief (few cm in outcrop) and the lack of karst cement indicate emersion of short duration lasting only a few centuries to a millennium (Farabegoli et al., 2007).

In more continuous sections, the basal Tesero Member is represented by 10–20 cm of ooid grainstone with abundant reworked and non-reworked micro- and macrofossils. A slight reduction in species richness, disappearance of large brachiopods and appearance of Lilliput taxa (e.g., *Bellerophon vaceki*; Twitchett, 2007) herald the early effects of the extinction (Knoll et al., 2007). The mass extinction peak is located about 29–45 cm above the Bellerophon–Werfen Formation (BWF) boundary at the appearance of concentric ooids (Fig. 4D, E; Bosellini, 1964; Broglio Loriga et al., 1988; Farabegoli et al., 2007; Groves et al., 2007; Posenato, 2009, 2010), and is located within the latest Changhsingian *Hindeodus praeparvus* Zone (Farabegoli et al., 2007). The Permo-Triassic boundary (PTB) at the Bulla section is placed 1.3 m above the BWF boundary (Perri and Farabegoli, 2003). The last Permian microfossils (calcareous algae and foraminifera) disappear in the lower *H. parvus* Zone (basal Triassic) at about 80 cm above the boundary in the Bulla section (Farabegoli et al., 2007; Posenato, 2010). Also at this section, the Tesero Member is overlain and intercalated with sediments of the Mazzin Member. The Tesero ranges from 30 to 40 m in thickness in near-shore settings of the southwestern Dolomites, to zero in the northeastern Dolomites and Carnia, where offshore silty marls and marly mudstones of the Mazzin Member represent the basal Werfen Formation (Assereto et al., 1973; Farabegoli and Viel, 1982; Broglio Loriga et al., 1983; Farabegoli et al., 2007). The Mazzin Member records devastation of the marine ecosystem by the appearance of an oligotypic benthic community dominated by the survivor taxa *Lingula* and *Unionites* (Broglio Loriga et al., 1988; Wignall and Hallam, 1992; Posenato, 2009).

High-resolution correlation between the lower Tesero Member and the lower Yinkeng Formation of the Meishan GSSP is difficult for several reasons: 1) the latter section is condensed, and its sedimentation rate appears to be much lower than that in the Dolomites, 2) in the Meishan section unconformities may exist within the PTB bearing layer (Bed 27; Cao and Shang, 1998; Chen et al., 2009), and 3) conodonts are rare in the Southern Alps. For these reasons different correlations schemes have been proposed between the two localities. For instance in Italy, the lower Tesero Member (*H. praeparvus* and *H. changxingensis* Zones), is correlated either to Beds 27a and 27b (Farabegoli et al., 2007) or to Beds 25 through 27b at Meishan (Posenato, 2010). Following Posenato (2010), we favor the latter interpretation and apply it for correlating between the sections of northern Italy and of Meishan, China.

4. Diagenetic evaluation

Prior to using any carbonate and its geochemistry in the reconstruction of paleoenvironmental conditions, the preservation potential of each sample must be evaluated by as many screening tests as possible (cf. Brand et al., 2011). Screening of our samples involved optical and petrographic inspection, cathodoluminescence, scanning electron microscopy of microstructures, trace element contents, and carbon, oxygen and strontium isotope compositions. Diagenesis may alter the total geochemistry, or only one, two, or several of the chemical constituents of the carbonate material (Brand, 2004; Brand et al., 2011). Biogenic low-Mg calcite (bLMC) holds great promise for preservation because it is thermodynamically the most stable carbonate at STP, although alteration is possible in diagenetic systems ranging from low to high water-rock ratios (Brand and Veizer, 1980, 1981; Banner and Hanson, 1990; Brand, 2004).

4.1. Screening of Sass de Putia carbonate components

Cathodoluminescence evaluation of the carbonates from Sass de Putia shows no luminescence of the brachiopods except for the peripheries (Fairchild, 1983; Barbin and Gaspard, 1995). It is mostly the inner 'core' or the 'secondary–tertiary' layers of the shells that do not luminesce (Fig. 5C1, C2). For this reason, and because the isotopic composition of the primary layer is also subject to a vital effect (Carpenter and Lohmann, 1995; Merkel et al., 2009), the outermost layer of brachiopods is routinely removed during sample preparation. Except for a few areas of geopetal micrite within the fossils, whole rock material exhibited dull to bright luminescence. Based on standard observations and interpretations, dull and bright luminescence indicates diagenetic alteration of the mineralogy and geochemistry of the studied whole rock carbonate (Fairchild, 1983). Additional screening of the carbonate material involved SEM scanning of microstructures within brachiopod fragments. Most scanned specimens exhibit fibers of the secondary layer with excellent preservation (e.g., Fig. 6A, B), and in some instances show stepped laminations in the tertiary-layer prisms (Fig. 6C, D); all clear indicators of microstructural brachiopod low-Mg calcite preservation (cf. Goetz et al., 2009; Merkel et al., 2009).

Further diagenetic evaluation involved the comparative screening of trace chemistry and isotopic compositions of brachiopod LMC and whole rock (Brand, 2004; Brand et al., 2011). The chemical content of previously deemed preserved brachiopods (based on cathodoluminescence) is high for Sr and low for Mg, whereas

Author's personal copy

Table 1
Stratigraphic distribution at the genus level of calcareous algae, foraminifera and brachiopods at Sass de Putia. Foraminifera and calcareous algae distributions from Broglio Loriga et al. (1988), and of brachiopods from Posenato (2001, 2011). Abbreviations: wPK, samples from the western Sass de Putia section (Fig. 3); PK, Sass de Putia section sampled by Broglio Loriga et al. (1988) and located about 100 m eastwards. Distances are in cm from the formational boundary, which is placed between beds wPK10B and wPK11A.

	wPK	3	5	7	8	9	10A	10B	11A	11B	12	12A	12B	
	PK	46E	47	48	49	50	51	52	53	54	55	56	57	61–62
	Distance	−130	−110	−85	−65	−40	−20	−5	5	12	22	35	60	160–200
Rhodophyta	Solenoporaceae ind.								X					
	Gymnocodium		X	X		X	X	X	X	X		X		X
Chlorophyta	Atractyliopsis	X	X	X		X	X							
	Mizzia	X					X	X	X	X	X			
	Macroporella		X					X						
Foraminiferida	Ammodiscus		X	X										
	Glomospira	X												
	Glomospirella	X		X				X						
	Robuloides					X	X							
	Nodosaria					X	X							
	Frondina					X	X	X						
	Geinitzina		X	X	X	X	X	X	X	X	X	X		
	Pseudoendothyra								X	X				
	Reichelina					X	X							
	Staffella							X	X	X	X			
	Sichotenella						X							
	Nankinella				X	X	X	X	X	X	X	X		
	Paradoxiella					X	X	X						
	Nanlingella							X						
	Wanganella					X	X	X						
	Colaniella					X	X							
	Globivalvulina		X	X		X		X						
	Paraglobivalvulina						X	X	X	X				
	Praglobivalvulinoides							X						
	Dagmarita							X		X				
	Agathammina		X					X	X					
	Baisalina		X					X			X			
	Hemigordius		X		X	X		X	X	X	X			
	Palaeonubecularia		X											
Brachiopoda	Comelicania		X	X			X	X						
	Comelicothyris							X	X					
	Janiceps							X	X	X				
	Ombonia							X	X	X	X			
	Orthothetina							X	X	X				
	genera	4	11	7	3	14	15	23	14	12	7	3		1

progressively altered brachiopod samples show concomitant decreases in Sr and increases in Mg (cf. Brand and Veizer, 1980). The Sr contents of the whole rock material is even lower than that of altered brachiopods, at the same time its Mg contents are the highest, clearly indicative of a high degree of alteration and in some instances of dolomitization (Fig. 7A, Appendix 1). Manganese and iron contents may increase with carbonate diagenesis, and as expected, the well-preserved material clusters close to the lowest values (Fig. 7B; cf. Brand and Veizer, 1980). The interpretation of carbon and oxygen isotopes is more complex, because local–regional environmental variations as well as secular shifts in seawater may result in different values for material from different horizons. In addition, accounting for more enriched carbon and oxygen isotopes in the 'original' aragonite (e.g., Sandberg, 1983; Stanley, 2006), constituting most whole rocks during this time period, would shift their 'primary' values by up to −1.85‰ and −0.8‰ for $\delta^{13}C$ and $\delta^{18}O$, respectively (e.g., Rubinson and Clayton, 1969; Tarutani et al., 1969). This is clearly demonstrated by the sample material from the two horizons of the Sass de Putia section. The preserved bLMC from horizon wPK3 and their $\delta^{13}C$ values cluster about +5‰ and their $\delta^{18}O$ values about −2.5‰, whereas the altered bLMC shows a slight negative displacement in $\delta^{18}O$. In contrast, the whole rock sample experienced, similarly, a slight shift in $\delta^{18}O$ but a large one in $\delta^{13}C$ relative to those of the unaltered bLMC (Fig. 7C).

The microstructurally preserved brachiopod bLMC from horizon wPK11A has more negative $\delta^{13}C$ and $\delta^{18}O$ values than those of the altered materials from horizon wPK3. This clearly demonstrates that screening for diagenetic alteration must be done for samples from each horizon separately and not as a 'lumped' population that includes all data, to account for local environmental variation and other influencing factors. Evaluation of sample material from each and every sample horizon allows us to differentiate between environmental and secular changes versus diagenetic alteration trends (cf. Brand, 2004; Brand et al., 2012a). The preserved brachiopod $\delta^{13}C$ and $\delta^{18}O$ values from horizon wPK11A cluster close together, whereas their altered counterparts show great scatter. In contrast, the $\delta^{13}C$ of the whole rock appears to have been preserved whereas its $\delta^{18}O$ value has not, which can happen in diagenetic systems with low water-rock ratio (Fig. 7C; Brand and Veizer, 1981; Veizer, 1983).

Strontium isotopes are sensitive to alteration in all types of diagenetic fluids and systems (Brand et al., 2010). The material from Sass de Putia is no exception; in all cases altered brachiopods contain more radiogenic Sr than unaltered counterparts (Fig. 7D). However, the greatest shift in radiogenic Sr is exhibited by the whole rock samples from both horizons, and thus they reflect alteration and are clearly unsuitable material for reconstructing original seawater-^{87}Sr curves.

4.2. Screening of Val Brutta carbonate components

Cathodoluminescence (CL) shows that unaltered brachiopods are non-luminescent (Popp et al., 1986; Brand et al., 2012a) and show similar CL results for the material from Sass de Putia; rims show some luminescence (Fig. 5D, E). In addition to the outer rims of brachiopod valves, whole rock for the most part shows dull to bright luminescence. Only micrite in some exceptional localities (intragranular cavity fill; Fig. 5E) or the rinds of allochems (Fig. 5F) do not luminesce. Overall, most of the bLMC of brachiopods does not luminesce, and thus, are deemed to

Author's personal copy

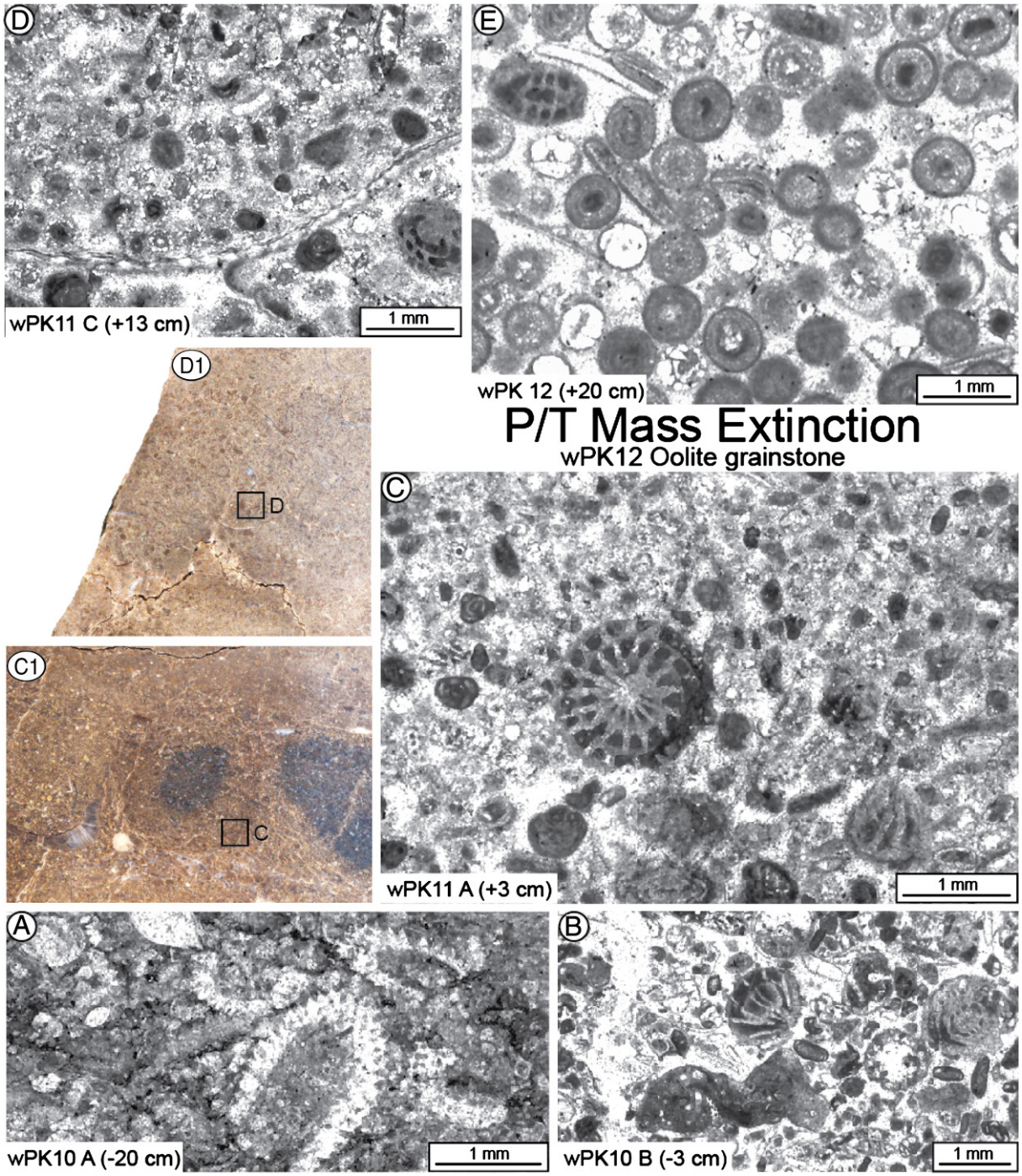

Fig. 4. Microfacies and polished sections from about the Bellerophon/Werfen formational boundary at Sass de Putia. A, B, Bulla Member, Bellerophon Fm; A, bioclastic wackestone rich in algae, fusulinids and organic matter; B, bioclastic wackestone/grainstone with reworked litho- and bioclasts. C–E Tesero Member, Werfen Formation; C, calcite coated peloid and ooid grainstone with unreworked and reworked bioclasts (a reworked fusulinid in the centre). Position of photomicrograph 'C' is shown in handspecimen C1; D, ooid grainstone with a sectioned *Ombonia* valve in the lower part. Position of photomicrograph 'D' is shown in handspecimen D1; E, oolite grainstone with a reworked fusulinid (upper left corner). Distance refers to the Bellerophon/Werfen Formational boundary.

be well preserved in their original mineralogy, whereas the carbonate of the whole rock with its dull to bright luminescence has undergone mild to extensive diagenetic alteration. However, further screening tests are necessary to confirm the observation based on CL for bLMC and whole rock, because Mn and Fe both increase with diagenesis (cf. Brand and Veizer, 1980), but only Mn may cause luminescence whereas Fe may suppress it (e.g., Fairchild, 1983).

Scanning electron microscopy screening of brachiopod shell fragments supports the CL evaluation that most of them are preserved in their original bLMC mineralogy. Scans of brachiopod fragments from Val Brutta show excellent preservation of fibers of the secondary layer (Fig. 6E) as well as of prisms of the tertiary one, with many showing the primary feature of 'stepped' lamination (Goetz et al., 2009; Merkel et al., 2009) within individual prisms (Fig. 6E–H).

Chemical screening of Val Brutta samples shows that Sr and Mg contents of the microstructurally and CL-based well-preserved brachiopods form a tight cluster, whereas the whole rock materials are enriched in Mg and depleted in Sr, suggesting that the former

Author's personal copy

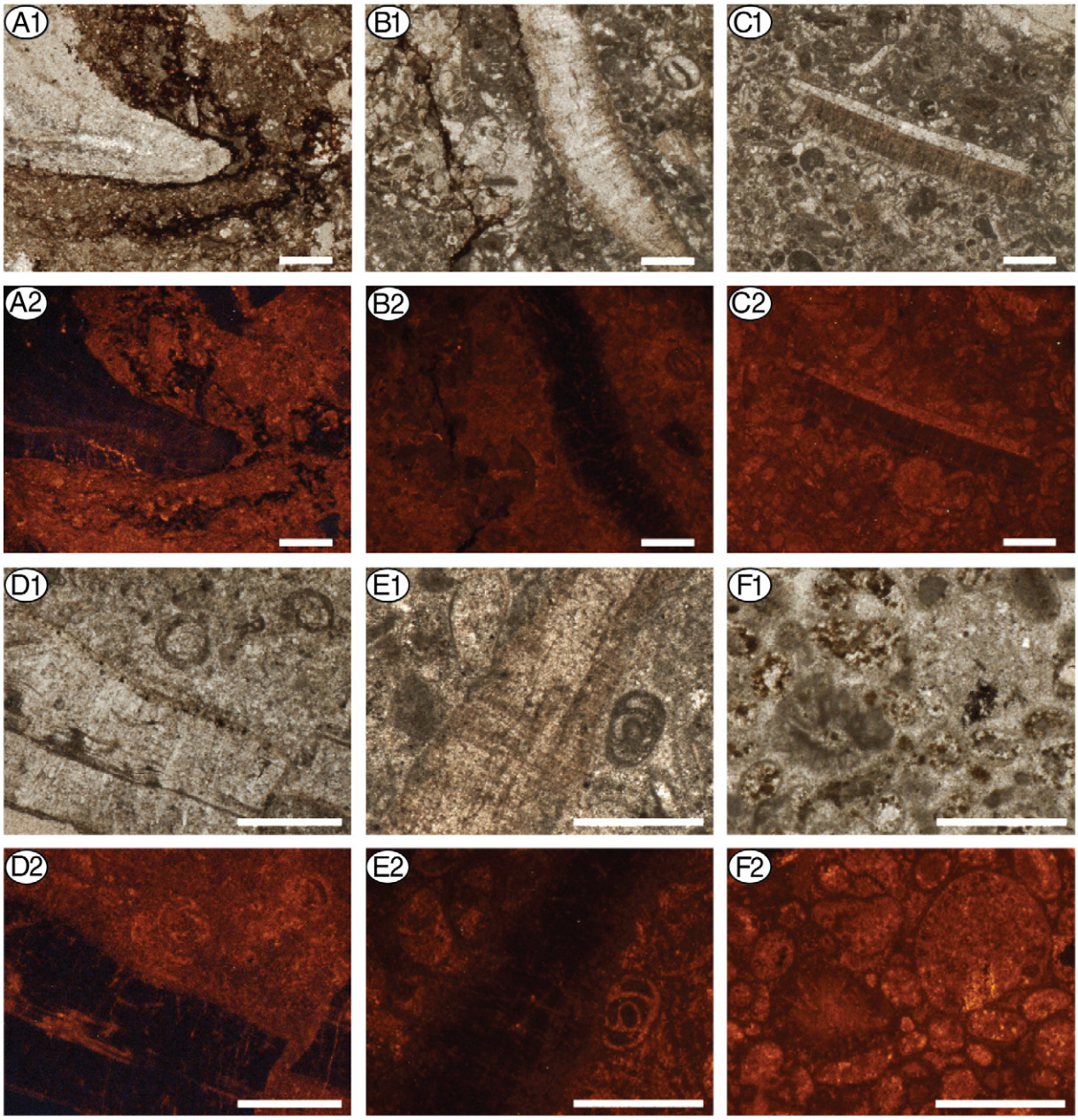

Fig. 5. Plane polarized light and cathodoluminescence petrography of select samples from Sass de Putia and Val Brutta, northern Italy. A1 and A2 are plane polarized light and cathodoluminescence thin sections of sample wPK5 top; B1 and B2 are corresponding plane light and cathodoluminescence sections of sample wPK10B; C1 and C2 are corresponding plane light and cathodoluminescence sections of sample wPK10B (different part of section); D1 and D2 are corresponding plane light and cathodoluminescence sections of sample VB9A; E1 and E2 are corresponding plane light and cathodoluminescence sections of sample VB10; and F1 and F2 are corresponding plane light and cathodoluminescence sections of sample VB11. Note: scale bar for all sections is 0.1 cm.

represent pristine material and the latter are diagenetically altered (Fig. 8A; Brand and Veizer, 1980). Primary carbonates usually contain low amounts of Mn and Fe, whereas with progressive diagenesis these contents tend to simultaneously increase in diagenetic ones. The bLMC of the brachiopods are low in Mn and Fe whereas their coeval whole rock are significantly enriched in both elements, which lends further support to the suggestion that the bLMC mineralogy and chemistry are pristine but that of the whole rock are not (Fig. 8B; cf. Brand, 2004).

The carbon and oxygen isotope compositions of brachiopods and whole rock from Val Brutta horizons 8A and 9C define five distinct groups (Fig. 8C). Some of the isotopic variation may be a reflection of changes in environments of deposition for the different horizons with time. Diagenesis in the presence of meteoric water may lead to a shift towards more negative values with progressive alteration, and in both instances the whole rock from both horizons exhibit this expected shift (Fig. 8C; Al-Aasm and Veizer, 1982; Brand and Veizer, 1981). Two of the brachiopod results from horizon VB9C are slightly negative in $\delta^{18}O$ and $\delta^{13}C$, which may reflect local environmental variations (Carpenter and Lohmann, 1995; Brand et al., 2003), we chose to exclude them from the environmental database to maintain consistency. Strontium isotopes support the preservation of the brachiopod bLMC but not of the whole rock material that is significantly enriched in radiogenic strontium (Fig. 8D; Brand et al., 2010).

Overall, the screening results give rise to three categories of preservation of the carbonate components studied from Sass de Putia and Val Brutta (Appendix 1). The geochemistry of only pristine material is used as proxy material to reconstruct 'primary' end of the Permian seawater isotope and temperature curves.

Author's personal copy

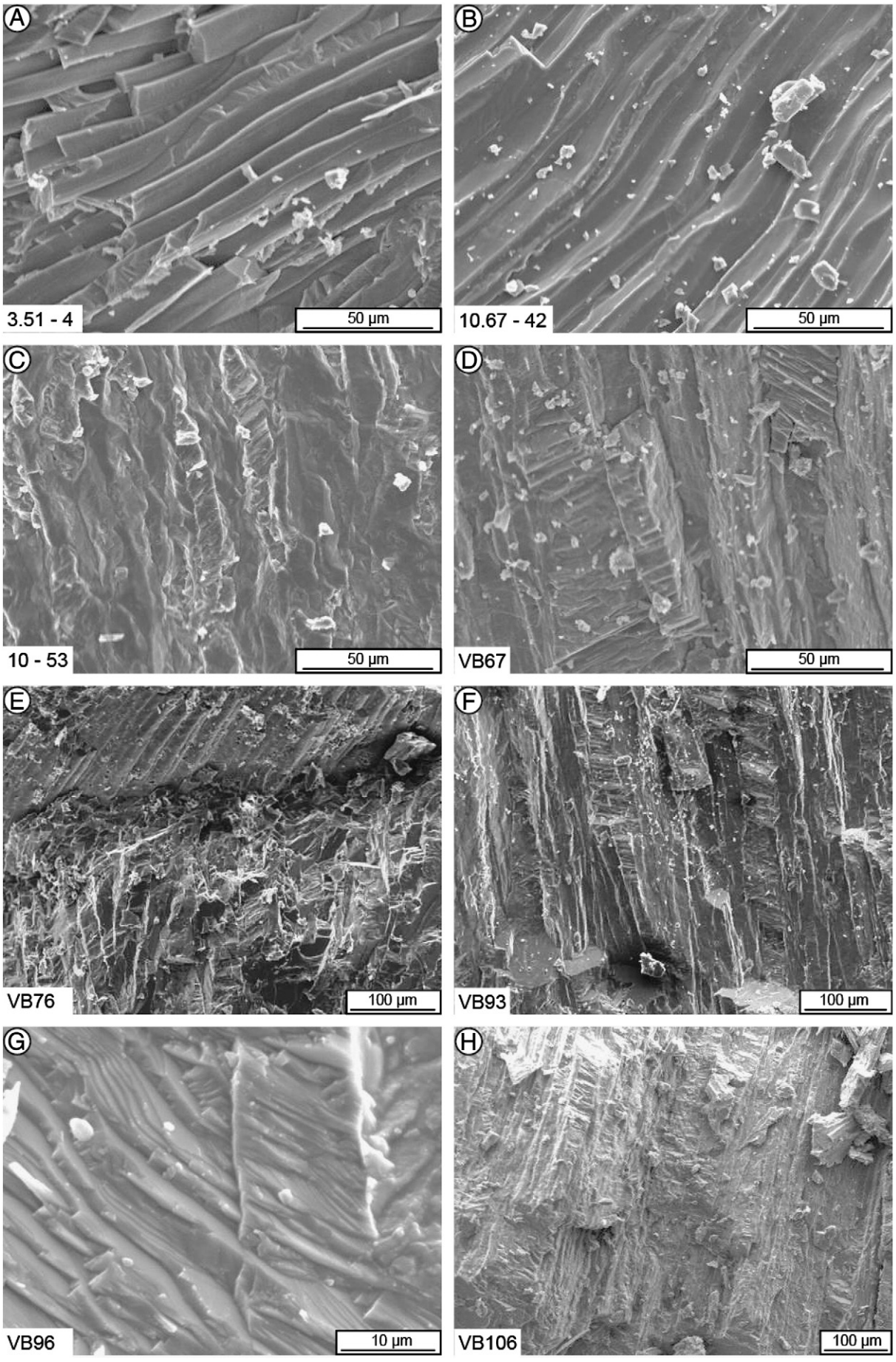

Author's personal copy

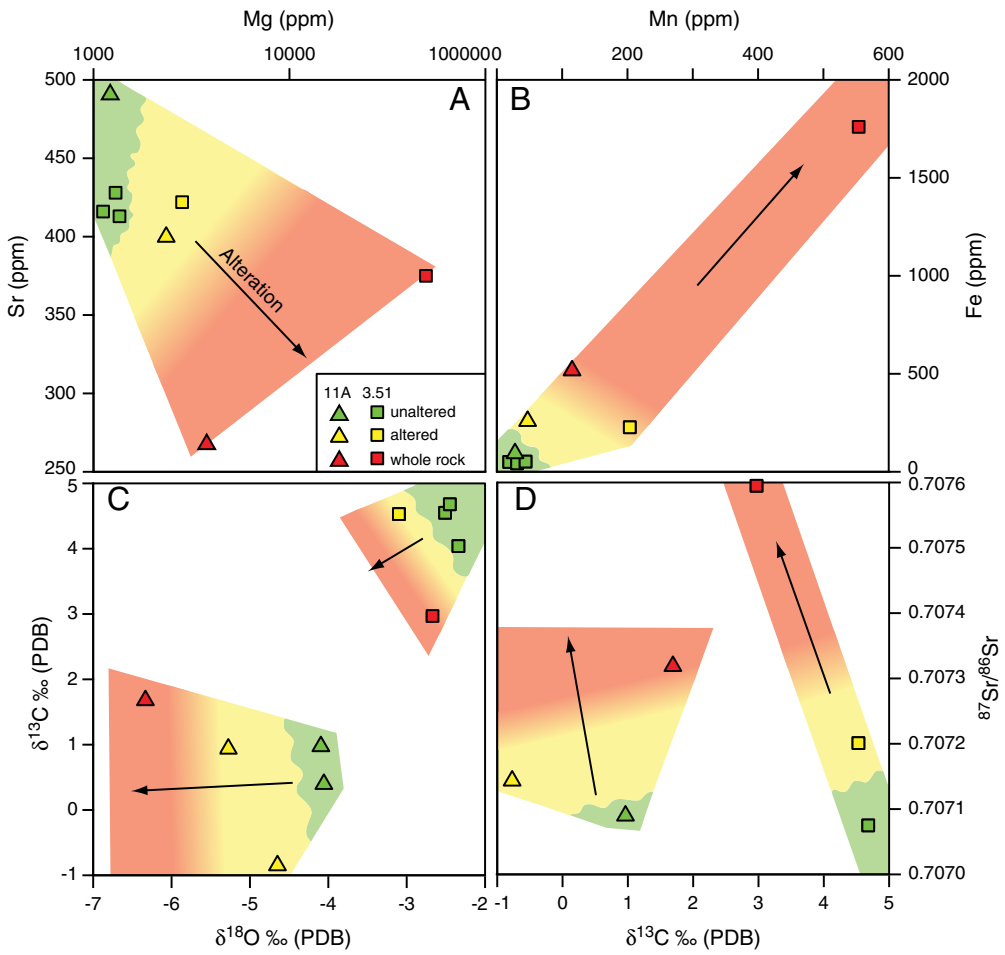

Fig. 7. Diagenetic evaluation of carbonates from Sass de Putia, northern Italy. A—Strontium and magnesium evaluation of the various carbonate components (brachiopods—unaltered and altered, whole rock) from horizons wPK3 (squares) and wPK11A (triangles; Appendix 1). Samples within the 'green' field are well preserved with original chemistry (elements and isotopes), whereas those in the transitional 'yellow to red' field have undergone variable degrees of diagenetic alteration (Brand, 2004; Brand et al., 2011). B—Iron and manganese evaluation of the carbonate components. C—Carbon and oxygen isotope evaluation of the various components (whole rock constituents are not adjusted for mineralogical enrichment). D—Strontium isotope evaluation of the various carbonate components from horizons wPK3 and wPK11A. (For interpretation of the references to color in this figure legend, the reader is referred to the web version of this article.)

5. Chemostratigraphy results of Northern Italy

Isotopic compositions of brachiopod bLMC (unaltered and altered) and of their coeval whole rock for the end Permian from northern Italy are presented in Figs. 9 and 10. The $^{87}Sr/^{86}Sr$ of the unaltered brachiopods from Sass de Putia and Val Brutta define a relatively invariant trend (Fig. 9A). There is minor overlap with values of altered brachiopods; otherwise the altered and whole rock results are much enriched in radiogenic strontium with no clear trend (Fig. 9A). The Sr isotope trend of the end of the Permian will be discussed further, in more detail (within the context of comparison with other sections).

The carbon isotope results of the material from Sass de Putia and Val Brutta, northern Italy depicts essentially the same trends: one for the low-Mg calcite and unaltered brachiopod and another one for the altered material and whole rock. The $\delta^{13}C$ of the brachiopods depicts a relatively invariant trend until close to the formational boundary (Bellerophon–Werfen) where it decreases dramatically into the Werfen (Fig. 9B). In contrast, with uncertainty about the original mineralogy of the whole rock, two sets of values are plotted ranging from aragonite (A) to low-Mg calcite (LMC) accounting for mineralogical fractionation (Fig. 9B; Rubinson and Clayton, 1969). Despite these adjustments, the whole rock $\delta^{13}C$ show only a gradual decline in values upward in the section, in contrast to the more abrupt change exhibited by the brachiopods.

Similarly, the $\delta^{18}O$ of unaltered brachiopods from Sass de Putia and Val Brutta define an invariant trend to just below the formational boundary where it declines rapidly (Fig. 9C). The oxygen isotope composition of the whole rock is depicted as two end members varying from aragonite (A) to low-Mg calcite (LMC) with appropriate adjustment for mineralogical fractionation (Fig. 9C; Tarutani et al., 1969). However, no clear trend is apparent for the $\delta^{18}O$ of the whole rock from the two Permian sections of northern Italy, instead they appear to represent both diagenetic and dolomitization processes (Fritz and Smith, 1970; Brand and Veizer, 1980; Banner and Hanson, 1990).

Based on the extensive screening of carbonate samples for preservation, only the best-preserved brachiopods were analyzed for their clumped isotope compositions (cf. Brand et al., 2011; Appendix 2). A total of eight samples from six horizons were analyzed for Δ_{47} resulting

Fig. 6. SEM microstructures within *Comelicania* from Sass de Putia and Val Brutta. A—shows well-preserved fibers of the secondary layer in the shell of *Comelicania* (#3.51-4, wPK3). B—is top view of well-preserved fibers of the secondary layer in sample #10.67-42 (wPK10A). C—well-preserved prisms with 'stepped' texture (laminae; Goetz et al., 2009; Merkel et al., 2009), other prisms along the periphery are coated by diagenetic cement (#10-53). D—tertiary prisms with 'stepped' texture indicative of excellent preservation (#VB67). E—boundary interval of well-preserved secondary layer fibers and prisms of the tertiary layer (#VB76). F—close up of well-preserved prisms of the tertiary layer (#VB93). G—stepped texture in prisms of tertiary layer of specimen #VB96. H—well preserved tertiary prisms in sample # VB106.

Author's personal copy

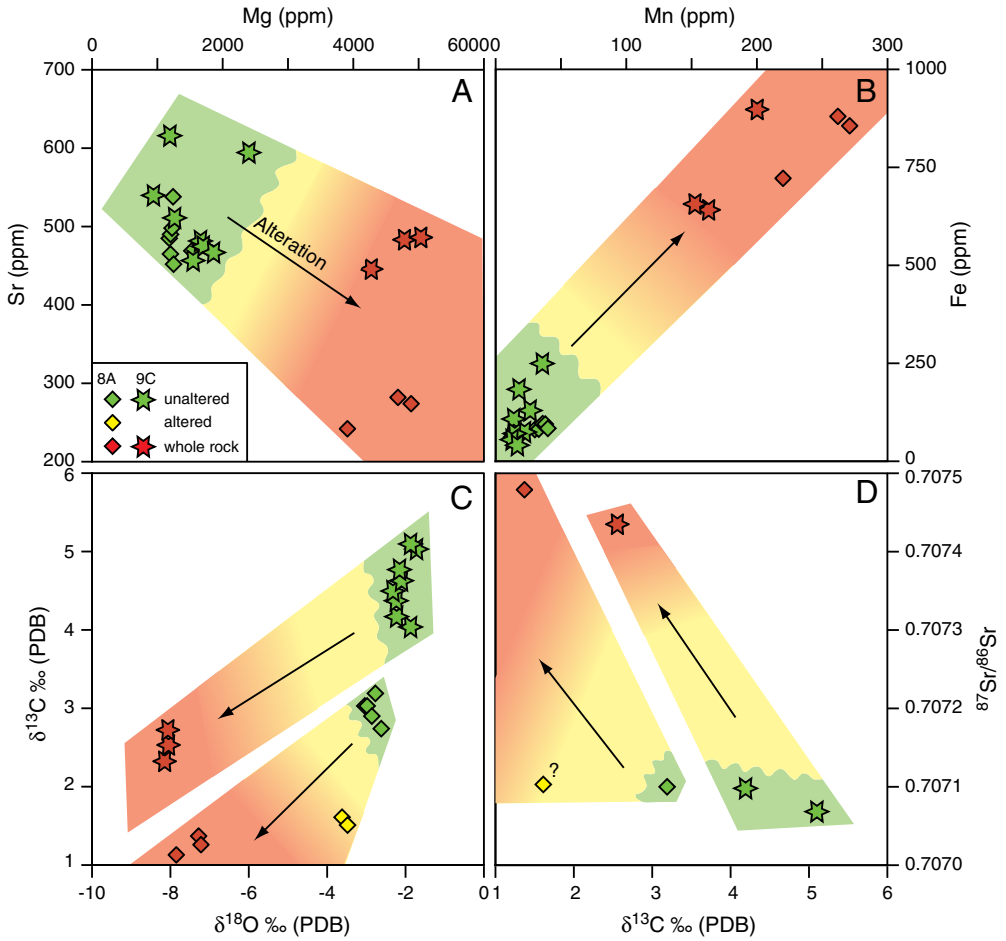

Fig. 8. Diagenetic evaluation of carbonates from Val Brutta, northern Italy. A—Strontium and magnesium evaluation of the various carbonate components (brachiopods—unaltered and altered, whole rock) from horizons VB 8A (diamonds) and VB 9C (stars; Appendix 1). B—Iron and manganese evaluation of the carbonate components. C—Carbon and oxygen isotope evaluation of the various components (whole rock constituents are not adjusted for mineralogical enrichment). D—Strontium isotope evaluation of the various carbonate components from horizons VB8A and VB9C. Color fields and their interpretations as in Fig. 7.

in values between 0.589‰ and 0.641‰ equivalent to 26°–39 °C (Ghosh et al., 2006). The resulting seawater $\delta^{18}O$ ranges from 2.0 to 0.7‰ (Fig. 10A). These high values are different from modern open-ocean or ice-free seawater but fall within the range of modern Caribbean and Red Sea seawater (Fig. 10A; Brand et al., 2012b). Seawater-^{18}O values derived from clumped isotopes for the end of the Permian of northern Italy suggest that the epicontinental western Tethys Sea may have been isolated from the open ocean at this time (cf. Brand et al., 2009), and/or it may have experienced evaporative conditions similar to those observed today in the Caribbean and Red Sea. Alternatively, the relatively ^{18}O-enriched seawater may reflect high mid-ocean ridge activity (e.g., Veizer, 1989; Korte et al., 2005, 2006), or combinations thereof.

Water temperatures based on clumped isotopes of the unaltered brachiopod LMC range from 30 to 38 °C (Appendix 2) with the lowest temperature close to the base of the sections and the highest being close to the extinction horizon (Fig. 10B). The global reconstruction of seawater temperatures will include temperatures calculated from carbonate $\delta^{18}O$ using the seawater-^{18}O compositions determined by clumped isotopes.

6. End-Permian chemostratigraphy—global comparison

High-resolution sampling was undertaken in the uppermost Bellerophon Formation and the lowermost Werfen Formation at Sass de Putia in the Italian Dolomites and at Val Brutta in the Venetian Prealps to facilitate comparison at the highest possible resolution with geochemical data from other end-Permian localities.

6.1. Strontium isotope comparison

The pristine bLMC from Sass de Putia and Val Brutta (the latter adjusted for different sedimentation rate) depict a $^{87}Sr/^{86}Sr$ curve that trends towards less radiogenic values up to about 15 cm below the BWF boundary (Fig. 11). At this level, a sharp reversal in the trend is observed with increasingly radiogenic values leading up into the extinction horizon (Fig. 11). In contrast, Sr isotope values of the corresponding whole rock samples are generally greater than 0.707300, more radiogenic than most of the brachiopods (outside the range of the figure), and well outside the natural seawater variation (indicated by the shaded band). Thus, based on all petrographic, CL and geochemical evidence, whole rock samples from Sass de Putia and Val Brutta do not contain a primary Sr isotope signal and are unsuitable for seawater composition reconstruction. Similarly, whole rock results from the Gartnerkofel Core-1, Austria (Kralik, 1991), from Meishan, China (Kaiho et al., 2001, 2006), the Meishan-1 core, China (Cao et al., 2009), and from Zagros, Iran (Wang et al., 2007) are all much more radiogenic than the coeval bLMC-^{87}Sr results of this study (Fig. 11), suggesting diagenetic alteration as the explanation for this wide range of values (cf. Kralik, 1991). Sr isotope values of conodonts from about the event and PTB in the Salt Range, Pakistan (Martin and Macdougall, 1995), as well as slightly older conodont-based Sr isotopes from Abadeh, Iran (Korte et al., 2004)

Author's personal copy

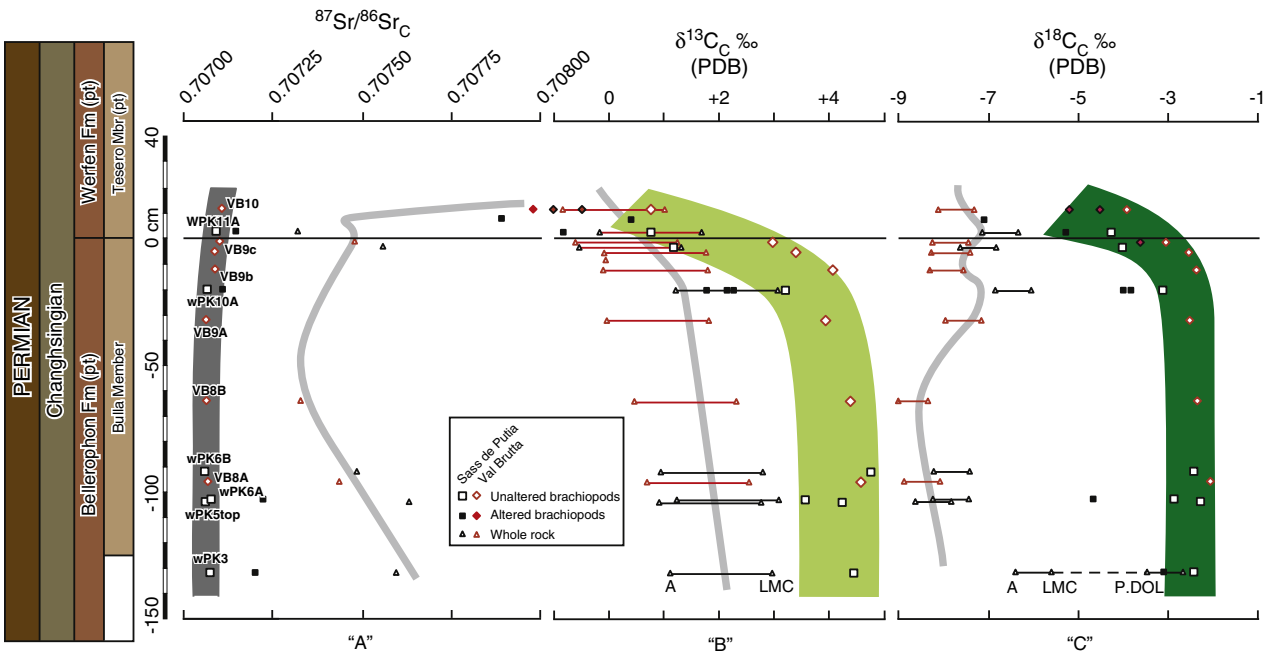

Fig. 9. Chemostratigraphy ($^{87}Sr/^{86}Sr$, $\delta^{13}C$, $\delta^{18}O$) during the end of the Permian in the Southern Alps, northern Italy. The whole dataset of unaltered and altered brachiopods and their coeval whole rock results are plotted with high stratigraphic resolution for the Bulla Member and lowermost Tesero Member. The isotopic compositions of the whole rock are represented by mineralogical ranges covering original aragonite (A) to low-Mg calcite (LMC). One whole rock sample is partially dolomitized (P.DOL; Appendix 1). The shaded band for the $^{87}Sr/^{86}Sr$ is based on the natural variation observed in modern brachiopods (Brand et al., 2003), whereas the bands of the $\delta^{13}C$ and $\delta^{18}O$ values represent the natural variation of all bLMC results from northern Italy (Appendix 1). Bands of the whole rock just define their overall trends.

are also quite radiogenic (Fig. 11). The Sr isotope values of the conodonts from the Salt Range are between 0.707309 and 0.707677, and this large variation is compounded by their relatively low stratigraphic (age) resolution. Thus, we suggest that the conodonts from Pakistan did not preserve pristine Sr isotope compositions.

Brachiopods from several localities (Spitsbergen, China and Iran) yield mixed Sr isotope values in addition to complicated stratigraphic assignments with the Bulla (Bed 24e at Meishan) and lowest Tesero (Bed 25 at Meishan) in the Southern Alps. The Sr isotope value of the bLMC from Spitsbergen (Gruszczynski et al., 1992) is more radiogenic (0.707647) than any values documented by its counterparts from northern Italy, and it is likely due to diagenetic alteration (cf. Mii et al., 1997; Brand, 2004). In contrast, two brachiopod-based Sr isotope results, one each from Iran and China (Korte et al., 2006), are consistent with the values obtained from the two sections in northern Italy. Although their values fall within the shaded band of the proposed end

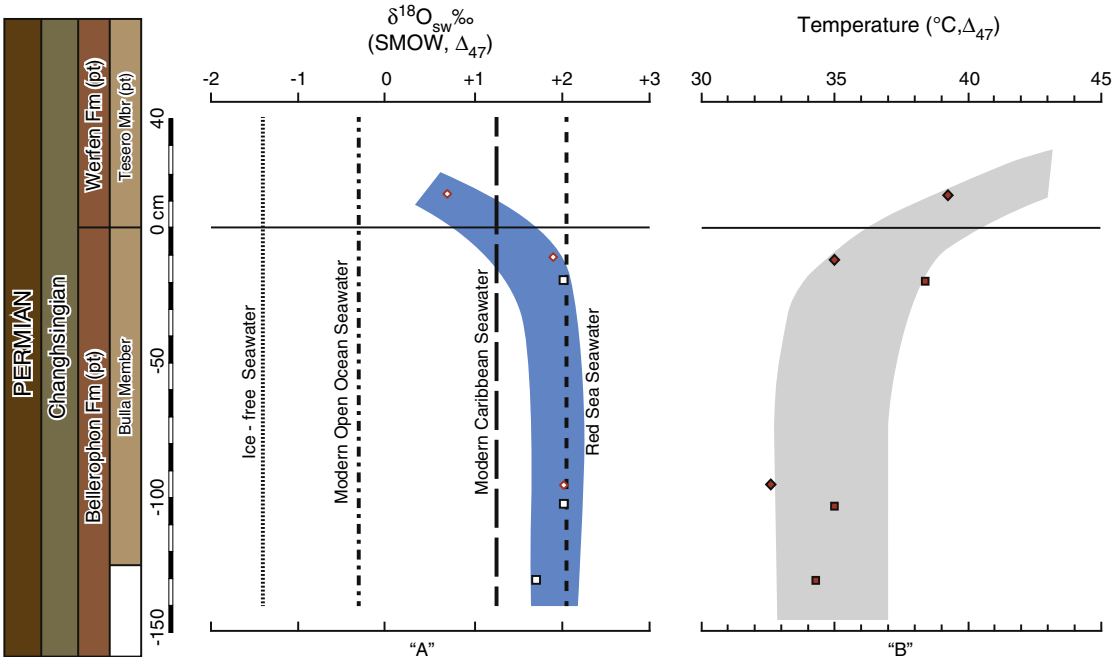

Fig. 10. Chemostratigraphy (SST and SSC-^{18}O) during the end of the Permian in the Southern Alps, northern Italy. Seawater $\delta^{18}O$ and SST are based on clumped isotopes (Δ_{47}) of unaltered brachiopod calcite from Sass de Putia and Val Brutta. The band of the SSC is based on the natural variation observed in modern seawater (Brand et al., 2003), whereas the temperature bandwidth is based on the total values computed with $\delta^{18}O_{carb}$ and seawater $\delta^{18}O$ values (Appendix 2). The seawater $\delta^{18}O$ values for ice-free, open-ocean are from Lhomme et al. (2005), Shackleton and Kennett (1975), respectively, and those of the Caribbean and Red Sea are from Brand et al., 2012b.

Author's personal copy

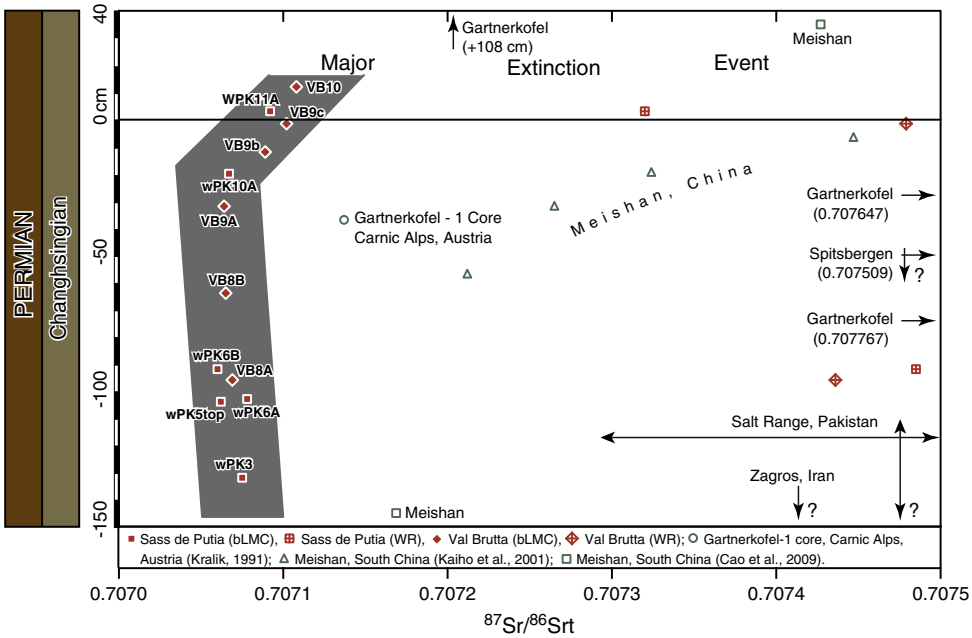

Fig. 11. Compilation of chemostratigraphic seawater $^{87}Sr/^{86}Sr$ data during the end of the Permian. The results of preserved LMC from Sass de Putia and Val Brutta have been merged into a singular trend (after adjustment for differential sedimentation rates, cf. Rampino et al., 2002; Groves et al., 2007; Posenato, 2009). For comparison, results of whole rock of this study are included on the diagram. Additional results are from: a) the Gartnerkofel-1 core, Carnic Alps, Austria (Kralik, 1991), b) Meishan, South China (Kaiho et al., 2001; Cao et al., 2009) c) Spitsbergen (Gruszczynski et al., 1992), d) Salt Range, Pakistan (Martin and McDougall, 1995), and e) Zagros, Iran (Wang et al., 2007). Stratigraphic uncertainty is identified by vertical bars about the symbol or 'stratigraphic' arrows with question marks. Results of other studies were also considered in this compilation but not plotted due to lack of analytical fidelity and stratigraphic robustness.

of the Permian seawater-^{87}Sr curve, their uncertain stratigraphic assignment makes their placement difficult (Fig. 11). The primary seawater-^{87}Sr values for the end of the Permian as defined by the shaded band reflects the variation observed in modern low-Mg calcite brachiopod counterparts (±0.000025, Brand et al., 2003). Thus, the high-resolution Sr isotope results from the Southern Alps provide the first evidence of highly non-radiogenic seawater close to the BWF boundary (or Bed 24e at Meishan), which is followed by a sudden change in the seawater-^{87}Sr trend just before the boundary (~15 cm) and continuing into and above the end-Permian mass extinction event (Fig. 11). Other than the data of Korte et al. (2006) and the bLMC data presented here, those of other studies (conodonts and whole rock), such as the Gartnerkofel (at +108 cm, 0.707207, Tesero +220 cm, 0.707213, Kralik, 1991), appear to be overprinted by post-depositional alteration processes and thus do not retain original seawater-^{87}Sr signals for the end of the Permian.

6.2. Carbon isotope comparison

Change in carbon isotope compositions has been traditionally used for characterizing both the end-Permian event as well as the PTB in the Alps and China (e.g., Holser et al., 1989; Xu and Yan, 1993; Yin et al., 2001) and at many other localities (e.g., Baud et al., 1989; Takahashi et al., 2009; Horacek et al., 2010; Korte and Kozur, 2010). However, there is considerable uncertainty as to whether changes in $\delta^{13}C$ were sudden, gradual, step-wise, or non-existent across these events (Jin et al., 2000). Furthermore, uncertainty persists as well as to the magnitude of the $\delta^{13}C$ shift, which may have varied by geography of sample material (cf. Retallack and Jahren, 2008). In some instances, brachiopod carbon isotope data (e.g., Gruszczynski et al., 1990) have been compared to whole rock values at the same and at other localities. These direct $\delta^{13}C$ comparisons between carbonates of different mineralogy, however, ignores the fact that different fractionation are associated with different minerals. For instance, the Late Permian was a time of aragonite (ARAG) dominated seas (e.g., Sandberg, 1983; Stanley, 2006) and thus for a direct comparison between ARAG and LMC isotope values, the former results need to be adjusted by about 1.85 ‰ to account for the typical ^{13}C enrichment in aragonite compared to calcite formed under the same conditions (Rubinson and Clayton, 1969). Similarly, dolomite may be enriched by several permil relative to coeval LMC (Fritz and Smith, 1970; Land, 1980). Consequently, all whole rock $\delta^{13}C$ results (of both previous studies and this one) have been adjusted by −1.85‰ to facilitate comparison with bLMC results (Fig. 12; e.g., Gruszczynski et al., 1989, 1990; Korte et al., 2005; Kearsey et al., 2009).

The $\delta^{13}C$ trend of the pristine bLMC from Sass de Putia and Val Brutta (including those of Kearsey et al., 2009) is invariant at approximately +4.0‰ (Korte et al., 2006) up to just 27 cm below the BWF boundary, and are confined to a band of ±0.9‰ that captures the observed variation (Fig. 12). The invariant $\delta^{13}C$ trend around +4.0‰ is followed by a rapid and negative shift to about +0.5‰ starting at about 27 cm below the BW formational boundary and continues into the lower Tesero at 0‰, marking the onset of the mass extinction event. A brachiopod from Meishan overlaps in $\delta^{13}C$ at the low end of the invariant trend (placed there due to reported stratigraphic uncertainty), but is similar to others from SE Sichuan (Fig. 12; Gruszczynski et al., 1990). Other brachiopod $\delta^{13}C$ results from SE Sichuan, China are assigned (due to reported stratigraphic uncertainty) to the middle of the mass extinction event, because placing them below would suggest that the materials are altered and placing them above the event would suggest that they are either altered or the event lasted longer than previously determined by all other means (Fig. 12). Another brachiopod from Sass de Putia (Korte et al., 2005) is similar in $\delta^{13}C$ to those of the lower Tesero Member at the onset of the mass extinction event (Fig. 12). Kearsey et al. (2009, p. 39) placed this sample "…just above the major phase of the mass extinction event…", however, no calcitic brachiopods were observed or found by us at horizons/levels after the extinction event in the Tesero Member at Sass de Putia or Bulla (Appendix 1). Thus, its position with respect to the seawater curves ($\delta^{13}C$ and $\delta^{18}O$) is relegated to the lower Tesero (Korte et al.,

Author's personal copy

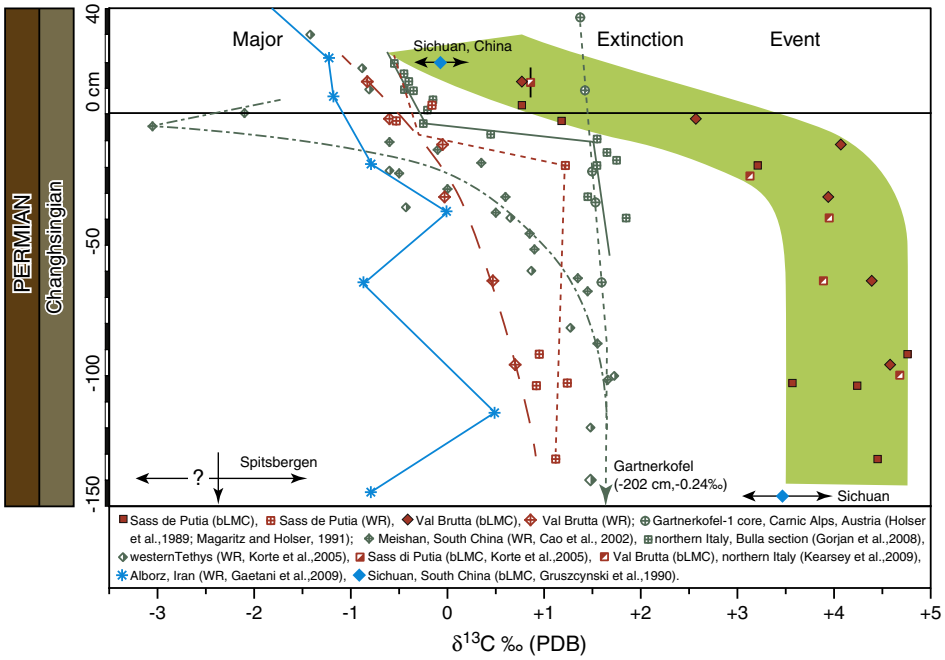

Fig. 12. Compilation of chemostratigraphic seawater-^{13}C data of the end-Permian. The results of preserved LMC from Sass de Putia and Val Brutta have been merged into a singular trend (cf. Rampino et al., 2002; Groves et al., 2007; Posenato, 2009). Additional results are from: a) the Gartnerkofel-1 core, Carnic Alps, Austria (Holser et al., 1989; Magaritz and Holser, 1991), b) Meishan, South China (Cao et al., 2002), c) Sichuan, China (Gruszczynski et al., 1990), d) Spitsbergen (Gruszczynski et al., 1989), e) northern Italy, Bulla section (Gorjan et al., 2008), f) western Tethys (Korte et al., 2005), and g) Val Brutta, northern Italy (Kearsey et al., 2009). All whole rock δ^{13}C values have been adjusted by −1.85‰ to account for mineralogical fractionation of the original material (Sandberg, 1983) and to facilitate comparison with δ^{13}C values of brachiopod LMC (Rubinson and Clayton, 1969). Results of other studies were also considered in this compilation but not plotted due to lack of analytical fidelity and stratigraphic robustness.

2005) and to the onset of the extinction event. Other latest Permian brachiopods from Spitsbergen exhibit δ^{13}C values (Gruszczynski et al., 1989) that are outside the realm of preserved material (Fig. 12), and this issue is compounded by their poor stratigraphic assignment. Therefore, we did not consider them in the reconstruction of the end Permian seawater-^{13}C curve.

Whole rock δ^{13}C results, after mineralogical adjustment of −1.85‰ (Rubinson and Clayton, 1969), are almost exclusively more negative than values of coeval pristine bLMC (Fig. 12). Furthermore, the magnitude of the pre-event 'shift' is highly variable ranging from 0‰ to about 5‰, and the trends themselves show variability that is similar in magnitude to the magnitude of the shifts (mostly negative with one positive across the event horizon; cf. Algeo et al., 2007). The whole rock δ^{13}C results from the various locations exhibit gradual shifts (e.g., Val Brutta, this study; Meishan, Cao et al., 2002), rapid shifts (e.g., Sass de Putia, this study; Bulla, Gorjan et al., 2008), or no shift (Gartnerkofel Core-1, Magaritz and Holser, 1991; Fio et al., 2010) in the δ^{13}C curve for the 1.5 m interval before and 40 cm during the event (Fig. 12). Only the trend of the δ^{13}C curve from Meishan observed by Cao et al. (2002), after accounting for the different sedimentation rates between China and the Alps, is similar to that exhibited by the bLMC from other localities (i.e., Italy), with the difference in magnitude being similar to the mineralogical offset. Results of other studies were not included in the figure because their trends mirror those already documented in Fig. 12 (e.g., Newton et al., 2004; Mu et al., 2009; Korte and Kozur, 2010), and their stratigraphic assignment is weak, and/or of low stratigraphic resolution (cf. Baud et al., 1989). Clearly, many different factors affect the carbon isotopic compositions of whole rock (cf. Heydari et al., 2001), which complicates the determination of a 'primary' value and trend, and impacts the consequent interpretations of the seawater-^{13}C curve preceding the end Permian. Based on pristine bLMC material, the δ^{13}C trend and subsequent shift leading into the end Permian mass extinction event was sudden and rapid over an interval of about 47 cm with a shift of about −4‰ in northern Italy (Fig. 12).

6.3. Oxygen isotope comparison

Oxygen isotopes are less commonly used to reconstruct the end-Permian mass extinction event and the PTB, because preservation of primary values, with few exceptions (cf. Brand and Veizer, 1980; Mii et al., 1997; Jaffres et al., 2007; Kearsey et al., 2009), is rare in carbonates from the Gartnerkofel-1 Core (Carnic Alps; Holser et al., 1989; Magaritz and Holser, 1991), Spitsbergen (Gruszczynski et al., 1989), SE Sichuan (China; Gruszczynski et al., 1990), and Northern Italy (Gorjan et al., 2008). To facilitate the comparison of δ^{18}O values between the presently LMC but originally aragonitic whole rock, and the low-Mg calcite brachiopods, the former were adjusted by 0.8‰ to account for their original mineralogical enrichment (Tarutani et al., 1969). This adjustment is made based on the generally accepted assumption that primary isotopic values are retained in the whole rock.

The δ^{18}O values of brachiopod LMC in this study and those of Kearsey et al. (2009) define a weak positive trend up to about 25 cm below the BWF boundary with values remaining within a narrow band (defined by the natural variation of the database) of approximately ±1.0‰ (Fig. 13). Subsequently, the δ^{18}O values trend abruptly negative and continue into the lower Tesero and the mass extinction event culminating in a most negative value of −5.9‰ for a brachiopod from SE Sichuan (Gruszczynski et al., 1990). Additional bLMC values from northern Italy are consistent with the curve but with lower stratigraphic resolution (Korte and Kozur, 2005; Korte et al., 2005). Other δ^{18}O values of brachiopod LMC from Spitsbergen are well outside the range of material deemed preserved, and are further complicated by their low stratigraphic resolution (Fig. 13).

All other data covering this time interval are more negative than those defining the high-resolution seawater-^{18}O curve. Furthermore, no specific trend in δ^{18}O is discernable in the other datasets except for the results from the Gartnerkofel-1 Core that shows a slightly decreasing trend towards the BWF boundary and a 1.5‰ negative excursion at about the boundary, and then a return to the previously established trend after the boundary (Fig. 13; Magaritz and Holser,

Author's personal copy

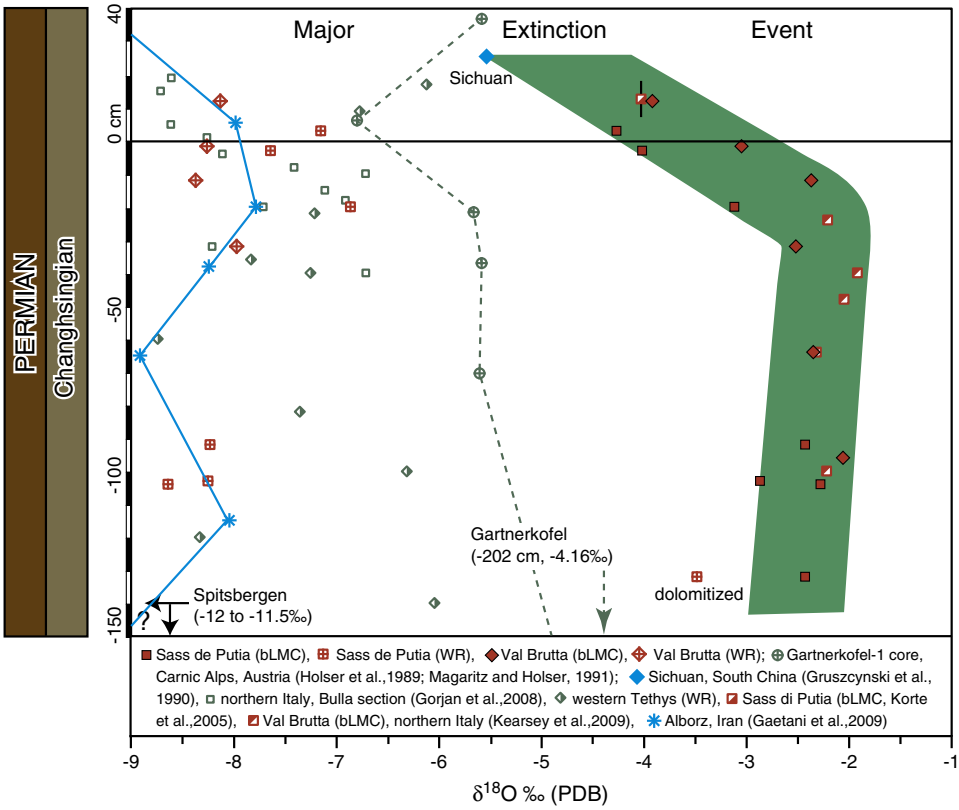

Fig. 13. Compilation of chemostratigraphic seawater-^{18}O data during the end of the Permian. The results of preserved LMC from Sass de Putia and Val Brutta have been merged into a singular trend (cf. Rampino et al., 2002; Groves et al., 2007; Posenato, 2009). Additional results are from: a) the Gartnerkofel-1 core, Carnic Alps, Austria (Holser et al., 1989; Magaritz and Holser, 1991), b) Sichuan, China (Gruszczynski et al., 1990), c) Spitsbergen (Gruszczynski et al., 1989), d) northern Italy, Bulla section (Gorjan et al., 2008), e) western Tethys (Korte et al., 2005), and f) Val Brutta, northern Italy (Kearsey et al., 2009). All whole rock δ^{18}O values have been adjusted by −0.8‰ to account for mineralogical fractionation and to facilitate comparison with δ^{18}O values of brachiopod LMC (Tarutani et al., 1969). Results of other studies were also considered in this compilation but not plotted due to lack of analytical fidelity and stratigraphic robustness.

1991). However, an excursion that is dependent on just a single value may reflect not a change in composition, but rather differential post-depositional alteration and/or mineralogical differences (Boeckelmann and Magaritz, 1991). Similarly, a partly dolomitized whole rock sample from Sass de Putia exhibits a δ^{18}O value that is more positive than its limestone counterparts analyzed during this study (Fig. 13). Dolomitization may increase δ^{18}O values of whole rock (Fritz and Smith, 1970; Land, 1980) and, thus, their inclusion in the reconstruction of a seawater-^{18}O curve is questionable.

7. End-Permian trends and causes

The Late Permian was a time of increased environmental stress with its elevated atmospheric pCO_2 and sea surface-water temperature (SST) reflected in the low biodiversity levels in the western Tethys (Broglio Loriga et al., 1988; Farabegoli et al., 2007; Posenato, 2009, 2010) and other localities (e.g., Shen et al., 2011b). This period of stress documented by biotic diversity decline was followed by a slight recovery towards the end of Bulla Member sediment deposition time (Posenato, 2010). Subsequently, this was followed by the greatest decline in marine and terrestrial biota during the end of the Permian (cf. Knoll et al., 2007). Some have suggested that the primary cause of the extinction of the Paleozoic biota was oceanic anoxia (e.g., Wignall and Twitchett, 1996), but it is difficult to explain the demise of the terrestrial biota through this mechanism (Benton et al., 2004; Ward et al., 2005; Retallack and Jahren, 2008). We will concentrate on evaluating the two competing hypotheses—oceanic anoxia and global warming—by characterizing global seawater isotope curves and their relationships to sea surface temperatures (SSTs), compositions (SSCs; Fig. 14) and atmospheric CO_2 concentrations.

7.1. Global oceanic anoxia

Anoxia has been proposed as a primary trigger of the end-Permian mass extinction, although the onset, and duration, and actual occurrence of anoxia are hotly debated (e.g., Wignall and Twitchett, 2002; Gorjan et al., 2007; Knoll et al., 2007; Shen et al., 2011b; Table 2). Our analysis of stratigraphically controlled redox sensitive indices such as U and Th, REEs, Ce anomaly and authigenic U on material from the two sequences of northern Italy (Jones and Manning, 1994), enable us to compare potential redox conditions of the western Tethys with those of South China, other Tethys localities and those of the Panthalassic Ocean. Shale normalized Ce anomaly values of less than unity indicate oxic/suboxic conditions whereas those of greater than unity reflect anoxic ambient water conditions (e.g., Bau and Dulski, 1996; Azmy et al., 2011). Evaluation of $(Ce/Ce^*)_{SN}$ values suggest that sediments and biota of northern Italy and Austria were deposited in oxic to suboxic waters during the late Permian (Fig. 14G), supported by their coeval authigenic U redox index (Appendix 2; Jones and Manning, 1994, Fig. 5). Only within the lowermost Tesero sediments at Sass de Putia, Val Brutta and Tesero, we observe a slight shift towards suboxic water conditions with $(Ce/Ce^*)_{SN}$ values approaching 1 (Fig. 14G), and slightly exceeding 1 in Slovenia (Dolenec et al., 2001). Ce anomaly values from a sequence in India suggest anoxia well before the event, but not immediately before or during it (Algeo et al., 2007). Similarly, sulphur and C_{org} contents of sediments from an adjacent section at Bulla in northern Italy (location #4, Fig. 2) support oxic seawater conditions during the Late Permian leading up to the end Permian mass extinction (Gorjan et al., 2007), although their specificity as a redox index is not always satisfactory (cf. Jones and Manning, 1994). However, the same study shows anoxic seawater conditions prevalent

Author's personal copy

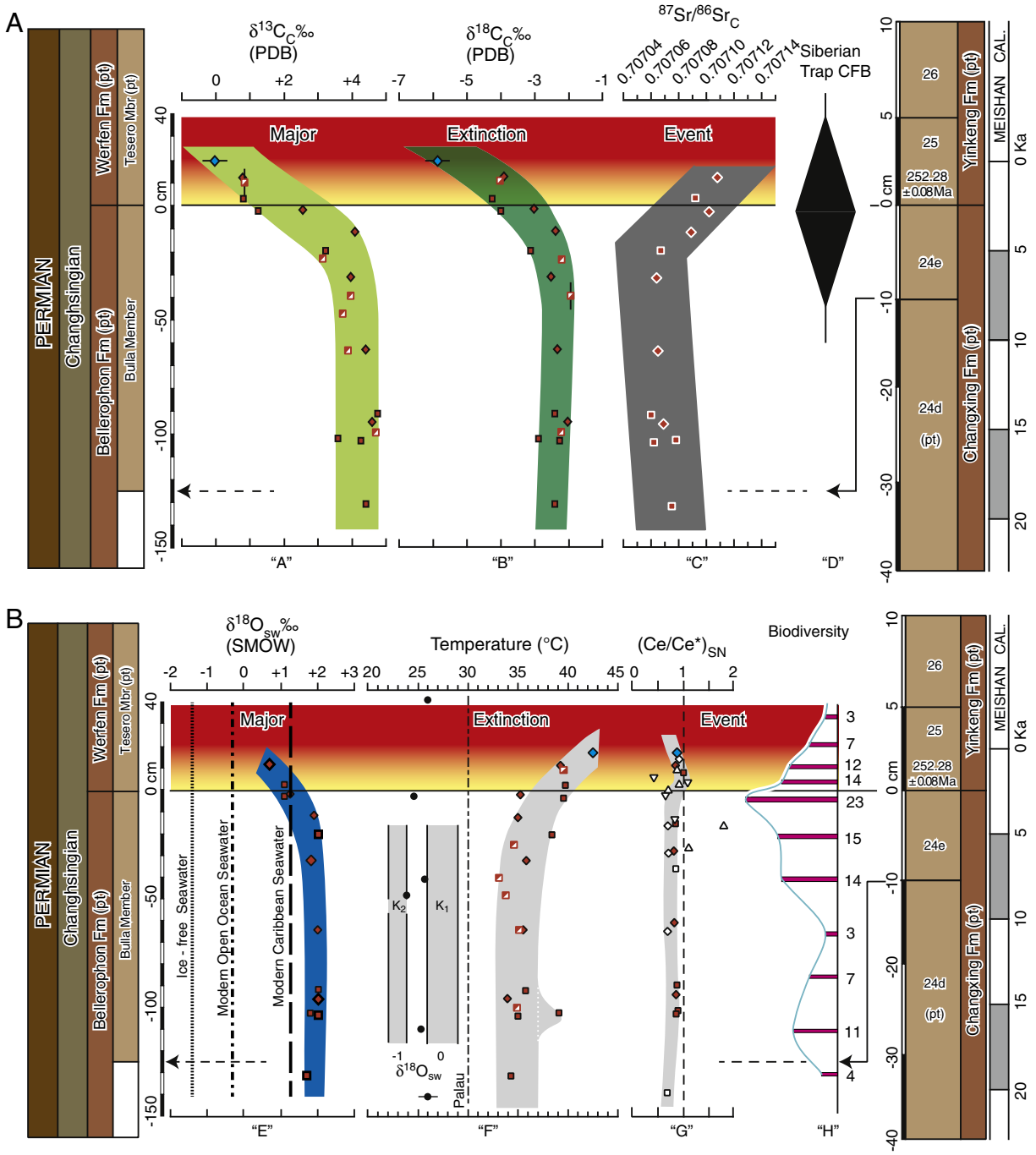

Fig. 14. A. High-resolution global seawater-^{13}C, SW-^{18}O, and SW-^{87}Sr curves during the end of the Permian. The seawater curves are based exclusively on brachiopod LMC from northern Italy (this study; Korte et al., 2005, 2006; Kearsey et al., 2009), and Sichuan, China (Gruszczynski et al., 1990). Stratigraphy of localities (northern Italy and Meishan, China) has been adjusted for different sedimentation rates (cf. Yin et al., 2001; Groves et al., 2007) based on U/Pb ages of Beds 22 (base; 252.50±0.11 Ma), 25 (mid; 252.28±0.08) and 28 (mid; 252.10±0.06 Ma) at Meishan, China (Shen et al., 2011a), and correlation of Bed 24e at Meishan, China to the Bulla Member of the Bellerophon Formation of Northern Italy (Posenato, 2010). $^{87}Sr/^{86}Sr$ values were all adjusted to a NBS-987 value of 0.710247. The bands about the values reflect their variation ($\delta^{13}C$, $\delta^{18}O$) or the natural variation ($^{87}Sr/^{86}Sr$) of modern counterparts (Brand et al., 2003). Eruption of the bulk Siberian Trap volcanic material occurred about the end Permian (Reichow et al., 2009). The 'Event Horizon' consists of lead-up conditions (yellow) and actual mass extinction conditions (red), and the Meishan age calibration (MEISHAN CAL) is based on ages of Beds 22 and 25, an inter-bed distance of 4.14 m (Shen, S. et al., 2011), and assumed constant sedimentation rate. B. High-resolution global seawater-^{18}O, sea surface temperature (SST), and sea surface composition (SSC-redox [Ce/Ce^*_{SN}]) curves related to biodiversity trend of the western Tethys area during the end of the Permian. The seawater $\delta^{18}O$ compositions are based on clumped isotope (larger symbol) and interpolated determinations (Appendix 2; Came et al., 2007), and the values for seawater in an ice-free, modern world and Caribbean are from Lhomme et al. (2005), Shackleton and Kennett (1975), Brand et al. (2012b), respectively. The sea surface temperatures (SSTs) are estimates (K_1, K_2) of end of the Permian tropical seawater (Kearsey et al. (2009), Palau SST (Colin, 2002), and end of the Permian seawater SST curve calculated with clumped isotopes and preserved LMC $\delta^{18}O$ values (Appendix 2; Came et al., 2007). The postulated water temperatures at Meishan (solid dots) are based on conodont $\delta^{18}O$ values and standard values for ambient seawater (Joachimski et al., 2012). The seawater redox curve is based on $(Ce/Ce^*)_{SN}$ values calculated with the Bau and Dulski (1996) formula and results of this study, Gartnerkofel, Austria (Attrep et al., 1991), Meishan, China (Zhou and Kyte, 1988), Slovenia (Dolenec et al., 2001), Croatia (Fio et al., 2010), and India (Algeo et al., 2011). The $(Ce/Ce^*)_{SN}$ values reflect changing seawater redox conditions (<1 = oxic, >1 = anoxic), and the biodiversity curve reflects changes in genera for the end of the Permian sea of northern Italy (Appendix 2, Table 1).

Author's personal copy

Table 2
Summary information on redox conditions of ambient seawater prior and during the end-Permian mass extinction.

Location	*Parameter*	*Observation/Evaluation*	*Source*
Western Tethys			
Sass de Putia, Val Brutta	Ce/Ce*	Oxic below event, suboxic–oxic during	This study (Fig. 14G)
Gartnerkofel-1 Core (GK-1, Austria)	Ce anomaly[1]	<1, below Tesero Member, oxic >1 uppermost Tesero, anoxic	Attrep et al. (1991)
GK-1 (Austria)	Biota, bioturbation	Mostly oxic conditions below event	Rantitsch (2007)
Suisi, Italy	$\delta^{34}S_{CAS}$	Anoxic after event	Newton et al. (2004)
Bulla, Italy	Benthic biota	Present up to the event, mostly oxic	Gorjan et al. (2008)
Bulla	S/C ratio	Oxic below event, anoxic during event	Gorjan et al. (2007)
Bulla	$\delta^{15}N$	Mostly oxic	Jia et al. (2012)
Tesero, Bulla, Suisi	Th/U	Anoxic above event	Wignall and Twitchett (1996)
Bletterbach, Italy	Biota, pyrite	L Tesero, oxic; upper Tesero, anoxic	Wignall and Hallam (1992)
South China			
Meishan D	Benthic biota	Oxic about event and PT boundary	Yin et al. (2001)
Meishan A	Benthic biota	Present into Bed 25, mostly oxic	Kaiho et al. (2006)
Meishan	Biota	No evidence of anoxia	Nicoll et al. (2002)
Meishan D	Ce* anomaly	<1, oxic to suboxic	Zhou and Kyte (1988)
Shangsi	Biota	No evidence of anoxia	Nicoll et al. (2002)
Ziyun	Coral reefs	Oxic (also at Laolongdond, S. China)	Cao et al. (2009)
Nanpanjiang	Benthic biota	Present below event, mostly oxic	Krull et al. (2004)
Meishan-1 Core	Pr/Ph	Anoxic	Cao et al. (2009)
Meishan A	$\delta^{34}S$, $\Delta^{34}S$	Shoaling of deep anoxic water	Shen et al. (2011a, 2011b)
Meishan	Th/U	Anoxic	Shen et al. (2011a, 2011b)
Tethys			
Medvodje, Slovenia	Th/U	Anoxic values above event	Wignall and Twitchett (1996)
Idrijca, Slovenia	Ce anomaly[1]	At 1 or <1, oxic–suboxic	Dolenec et al. (2001)
Rizvausa, Croatia	Ce/Ce*	<1, oxic	Fio et al. (2010)
Bükk, Hungary	Benthic biota	Mostly oxic	Haas et al. (2007)
N. Caucasus	Brachiopods	Mostly oxic	Ruban (2010)
Guryul, India	Ce/Ce*	Values vary about 1 ± 0.3	Algeo et al. (2007)
Guryul, India	Bentic biota	Oxic before event	Wignall et al. (2005)
Jiangyema, Tibet	Coral reefs	Oxic	Cao et al. (2009)
Panthalassic Ocean			
K. Starostin, Spitsbergen	Brachiopods	Mostly oxic	Mii et al. (1997)
K. Stosch, Greenland	Benthic biota	Mostly oxic	Stemmerik et al. (2001)
Sverdrup Basin	Pyrite, C_{ORG}	Alternating anoxic	Grasby and Beauchamp (2009)
Japan	Pyrite, C_{ORG}	Anoxic (deep sea sediments)	Isozaki (1997)
Japan	DOP, C & S	Mostly suboxic	Algeo et al. (2011)

Note: Shale normalized [1]Ce anomaly values calculated with formula of Bau and Dulski (1996).

during the extinction time period. Overall, chemistry and biota in northern Italy and Austria suggest that western Tethys surface seawater was prevalently oxic during pre-extinction time (Fig. 14G, Table 2). Seawater anoxia, based on a multitude of proxies, was noted in the uppermost Tesero, which places it well after the mass extinction event in sections from the western Tethys (Table 2, Fig. 3).

Results from South China almost exclusively suggest oxic to slightly dysoxic conditions up to and during the event (Bed 25, Table 2), with the exception of results from the most recent three studies (Cao et al., 2009; Shen et al., 2011a, 2011b). It is possible that seawater anoxia was not global but a local phenomenon and in upwelling regions. Observations, from other localities in the Tethys Sea suggest that seawater was generally oxic before the event and only slightly anoxic during the onset of the event in two localities (Fig. 14G, Table 2). These observations clearly support the notion that surface seawater anoxia, albeit slight, was a local phenomenon (Knoll et al., 2007).

Evidence of deep ocean water anoxia comes from Japan in the open Panthalassic Ocean (Isozaki, 1997). In contrast, the biota suggests that shallow seawater was mostly oxic in the Spitsbergen–Greenland area during the latest Permian (Table 2). Another study of deep sediments from the latest Permian of Japan suggests that deep bottom water of the Panthalassic Ocean was mostly suboxic during this critical time period (Algeo et al., 2011). This suggests that even deep waters of the Panthalassic Ocean were mostly suboxic at best and anoxic only locally (cf. Knoll et al., 2007). In summary, all available evidence from biota to geochemistry and supported by modeling (Zhang et al., 2001), from either shallow or deep water, suggests that latest Permian seawater was mostly oxic to dysoxic with only local cases of anoxia up to and including the mass extinction event. Therefore, the lack of global anoxia suggests that it is unlikely that it was the primary cause for the seawater-^{13}C isotopic shift prior to the event, nor a trigger of the end-Permian mass extinction.

7.2. Global warming—time constraint

Volcanism was a profound component of latest Permian and earliest Triassic time. Reichow et al. (2009) concluded that bulk volcanic activity at 250 Ma slightly predates, but overall was synchronous with the end-Permian mass extinction. It is documented in Bed 25 at Meishan with an Ar/Ar age of 249.83 ± 0.15 Ma (Renne et al., 1995; Jin et al., 2000; Reichow et al., 2009) and with a U/Pb age of 252.28 ± 0.08 Ma (Shen et al., 2011a) in the Bulla Member of the Bellerophon Formation of northern Italy (Posenato, 2010). The above reported age discrepancy may be related to inter-laboratory, calibration, and/or tracer solution bias (cf. Shen et al., 2011a).

The latest U/Pb ages of Beds 22, 25 and 28 in the Meishan section bracket the age of the PTB and the duration of the end-Permian mass extinction event (Shen et al., 2011a). Unlike Shen et al. (2011a) who favored using the ages of Beds 25 and 28 to establish a sedimentation rate for the succession at Meishan, we prefer using the ages of Beds 22 and 25 that precede and mark the extinction to determine sediment accumulation rates. Assuming a constant sedimentation rate, ages of 252.50 ± 0.11 (Bed 22) and of 252.28 ± 0.08 (Bed 25) yield an elapsed time of about 220,000 years for a cumulative sediment thickness of

Author's personal copy

4.14 m (Shen et al., 2011a), and a rate of 531.4 years/cm at Meishan. Applied to Bed 24e, this rate suggests duration of 5314 years, which is equivalent to 42.5 years/cm for the Bulla Member of the Bellerophon Formation of northern Italy (cf. Posenato, 2010).

Based on these ages and assuming constant sedimentation rates, we conclude that bulk Siberian volcanism preceded the extinction event by less than 10,000 years (e.g., Reichow et al., 2009), or possibly much less if the ages of Shen et al. (2011a) are strictly applied to this interval. Determination of this time interval is critical in the modeling of the pre-extinction $\delta^{13}C$ shift, and the associated atmospheric CO_2, SST and SSC changes (cf. Berner, 2002) that are pronounced at Meishan, China and northern Italy. Based on the 42.5 years/cm sedimentation rate for the Bulla Member, the shift in the seawater-^{13}C curve preceded the end-Permian mass extinction event by about 2000 years, the shift in the seawater-^{18}O curve by about 1900 years, and the shift in seawater-^{87}Sr by about 1500 years. The isotopic seawater curves will be presented and discussed in sequential order of changes/shifts preceding and impacting the mass extinction event.

7.2.1. Carbon isotopes (carbonate and seawater)

The Permian, with few exceptions, is characterized by a seawater $\delta^{13}C$ curve that is relatively invariant at about +4.0‰ (Korte et al., 2005) up to about 27 cm below the BWF of northern Italy or within 2.2 cm of the Bed 24e/25 boundary at Meishan, China (Fig. 14A). At that time, the $\delta^{13}C$ shifted suddenly toward negative values—over an interval of time that lasted less than 2000 years—right into the end—Permian mass extinction horizon (Fig. 14A). The duration of our $\delta^{13}C$ shift is at odds with those documented by previous studies, which includes estimates of <165,000 years (Bowring et al., 1998), to 60,000–10,000 years (Twitchett et al., 2001), <30,000 years (Rampino et al., 2002), and <20,000 years, Shen et al. (2011a). Furthermore, our age and trend are at odds with the gradual change in $\delta^{13}C$ of about 2.4‰ observed over the preceding 1.79 m (~90,000 years), which is not observed by us in the LMC-$\delta^{13}C$ from northern Italy Fig. 14A). Nor with the sudden shift of about 5‰ over the final 5 cm (<20,000 years) leading up to the event at Meishan by Shen et al. (2011a, p. 1368), which is an order of magnitude longer than the duration we observed. We attribute the difference between our results and the results of previous studies to our use of pristine bLMC, rather than whole rock material (e.g., Brand and Veizer, 1981; Brand, 2004; Knauth and Kennedy, 2009).

The observed $\delta^{13}C$ shift may have been produced by the oxidation of organic matter, by the emission of volcanic carbon dioxide, by the release of thermogenic methane or by a collapse in productivity, but not oceanic anoxia since it was already ruled out as a contributing factor (see Section 7.1). However, Berner (2002, 2005) who conducted extensive modeling of end of the Permian changes in seawater and atmospheric carbon and oxygen contents, concluded that the negative $\delta^{13}C$ shift preceding and continuing into the mass extinction event was not caused by organic matter burial or weathering, because both of these processes are too slow for this extremely rapid event. Similarly, volcanic eruptions occurring a time span of greater than 200,000 years would not have produced the sudden and rapid, large magnitude shift in $\delta^{13}C$ as observed for the end of the Permian (Fig. 14A; Berner, 2002). Instead, based on the volume of volcanic material produced by the 'bulk' Siberian volcanic activity at about 250 Ma, we suggest that rapid volcanism—with a discharge of CO2 over a time span of 10,000 years or less—could result in the rapid and large magnitude $\delta^{13}C$ shift of—4‰ at the end—Permian event (Fig. 14A; cf. Berner, 2002). Thermogenic methane-derived CO_2 may have been a contributing factor and because of its long atmospheric residence time would assist in shifting the seawater $\delta^{13}C$ curve and contribute to an appreciable geologic-time global warming component (Berner, 2005). Indeed, it is widely accepted that the Late Permian was a time of high atmospheric CO_2 content and a globally equable warm climate (cf. Kidder and Worsley, 2004), based, in part, on stomatal index studies of fossil plants (e.g., Retallack, 2001, 2002, 2009) and Siberian Volcanic-Trap LIP (large igneous province) produced CO_2.

7.2.2. Oxygen isotopes (carbonate)

If global warming was prominent during the end of the Permian, then a trend similar to that observed in carbonate $\delta^{13}C$ values should be also recorded in the coeval $\delta^{18}O$ of the pristine bLMC. This is indeed observed in the bLMC $\delta^{18}O$ curve from the end of the Permian sections of northern Italy, which lags the $\delta^{13}C$ curve by less than 100 years (Fig. 14A, B). Oxygen isotope values are relatively invariant between −3.0 and −2.0‰ up to 25 cm below the formational boundary, but subsequently $\delta^{18}O$ values become more negative to −5.9‰ (provided this is an unaltered result) during the peak of the event (Fig. 14B). Based on an ice-free world and a corresponding seawater composition of −1.4‰ (Lhomme et al., 2005), pre-event temperatures would have varied between 18 and 23 °C and increased to a maximum of 36° (using the calibration of Kim and O'Neil, 1997) during the peak of the event (Fig. 14B). In the absence of an actual seawater composition, the $\delta^{18}O$ of seawater must be assumed, and the resulting estimates of SSTs are not high enough to cause the massive end-Permian mass extinction (cf. Kearsey et al., 2009).

7.2.3. Strontium isotopes

We shall concentrate our effort on reconciling the geological, biological and primary geochemical evidence at hand to resolve the cause for the great end-Permian mass extinction. The Permian was a time of de-glaciation, massive oceanic plate tectonic activity responsible for assembly of Pangea, and opening of the Neotethys, and by the time the period came to a close the Paleozoic marine biota were replaced by a Modern fauna (Sepkoski, 1981). Based on a comparison to the time scale of South China (Shen et al., 2010) and the ages of Beds 22, 25 and 28 (Shen et al., 2011a), the high-resolution Late Permian interval covered in this study probably involved a period of <20,000 years (Fig. 14C; cf. Rampino et al., 2000, 2002).

Mid-ocean ridge (MOR) hydrothermal activity associated with opening of the Neotethys progressed through the Cisuralian and culminated in a low seawater $^{87}Sr/^{86}Sr$ ratio of 0.706857 near the end of the Capitanian (Korte et al., 2006) and a more ^{18}O-enriched seawater as a result of the hydrothermal flux (Veizer, 1989). A slight increase in the apparent seawater-^{87}Sr value to 0.707057 by the end Dzhulfian (Wuchiapingian) and a further increase to 0.707157 near the Permo-Triassic boundary suggest a slowing of tectonic rifting and/or seafloor spreading. However, the detailed chemostratigraphy of the carbonate succession in northern Italy leading up to the end-Permian mass extinction suggests that the $^{87}Sr/^{86}Sr$ ratio was actually decreasing or invariant from the end of the Dzhulfian (Wuchiapingian) to about 15 cm below the event at about 0.707060 (Fig. 14C). These Sr isotope values suggest low-level MOR hydrothermal activity during the Late Permian (Fig. 14C; e.g., Taylor and Lasaga, 1999). This trend in the seawater-^{87}Sr curve continued up to the last 15 cm of the Bulla Member, when it suddenly changed to radiogenic values leading into the lower Tesero and the end-Permian extinction event (Fig. 14C). This shift greatly lags the emission of voluminous carbon dioxide and gradual warming of the Earth (Fig. 14A, B). Eventually, CO_2 emissions must have facilitated the production of acid rain, which would have enhanced continental chemical weathering of silicate rock (e.g., Retallack, 1999; Retallack and Krull, 1999) leading the shift and trend of radiogenic seawater-^{87}Sr into the end of the Permian (Fig. 14C; MacDougall, 1988). This process sequesters atmospheric CO_2 (e.g., Taylor and Lasaga, 1999), produces negative shifts in $\delta^{13}C$ and promotes general cooling; but the geochemical evidence does not fully support this assertion. Indeed, there was a globally recognized negative shift in $\delta^{13}C$ during the end of the Permian (Fig. 14A) but warm SSTs, with one exception of short duration cooling, were the norm. Enhanced continental weathering and erosion (Retallack, 2005; Sephton et al., 2005) is a plausible explanation for this end of the

Author's personal copy

Permian radiogenic trend in seawater-^{87}Sr, but CO_2 uptake was counteracted by emissions leading to increasing atmospheric CO_2 levels and the global warming trend.

7.2.4. Seawater oxygen isotopes

The Late Permian was a time of warm equable climate and an essentially ice-free world (Racki and Wignall, 2005), and as such the oxygen isotopic composition of global open-ocean seawater should have been about −1.4‰ (Fig. 14D; Lhomme et al., 2005), assuming the average seawater composition of −0.3‰ for an interglacial modern world (Shackleton and Kennett, 1975). Without knowing the actual seawater composition, $\delta^{18}O$-derived water temperatures can only be estimated, and sometimes they disagree with modeled temperatures. Similarly, our pristine carbonate $\delta^{18}O$ values (ranging from −5.2 to −1.74‰ and assuming a seawater composition of −1.4‰ for an ice-free world), suggest a water temperature range of 16 to 32 °C (Kim and O'Neil, 1997) for the end of the Permian. This is similar to SSTs of the modern tropical ocean (cf. Colin, 2002; Brand et al., 2003), and surely insufficient to be a cause of the end-Permian mass extinction (cf. Knoll et al., 2007; Kearsey et al., 2009).

Clumped isotopes (Δ_{47}) can be used to determine carbonate growth temperatures, which are directly related to ambient seawater temperatures and together with primary carbonate $\delta^{18}O$ values allows us to calculate actual seawater $\delta^{18}O$ compositions (e.g., Ghosh et al., 2006; Came et al., 2007). The temperatures derived from clumped isotopes and $\delta^{18}O$ vary between 33° and 38 °C in the pre-event record and reach up to 42 °C (Sichuan material) during the peak of the end-Permian event (Appendix 2). Thus, seawater $\delta^{18}O$ derived from these temperatures, during deposition of the lower Bulla Member and up to just below the formational boundary was +2±0.3‰ SMOW (Fig. 14E) at Sass de Putia and Val Brutta in the western Tethys. This seawater composition persisted until about 25 cm before the BWF boundary, with a subsequent decrease to about +0.7‰ during the early phase of the mass extinction (Fig. 14E). This range of seawater-^{18}O compositions is similar to that found in the Caribbean and the Red Sea, and is reasonable for a sea after extensive hydrothermal activity (cf. Wallmann, 2001). Thus, for the first time, we have seawater $\delta^{18}O$ values spanning this critical part of Earth's history, allowing us to determine SSTs for the end of the Permian and for the mass extinction period.

7.2.5. Global sea surface temperatures

The Late Permian was without a doubt a time of warm and possibly hot climates, but magnitude of the warmth is highly uncertain. Holser et al. (1989) speculated, based on their oxygen isotope values of dolomites from the Gartnerkofel-1 core of Austria, that Late Permian SST must have been warmer by about 6 °C than today's tropical ocean. Since that publication, global water temperatures at the end of the Permian have been estimated as 10 °C or warmer than today, with up to 20 °C warmer in high latitudes (e.g., Grard et al., 2005; Kiehl and Shields, 2005; Korte and Kozur, 2005; Racki and Wignall, 2005). Kearsey et al. (2009) using pristine $\delta^{18}O$ values derived from LMC brachiopods and assuming water compositions of 0 or −1.0‰ determined SSTs ranging from 26–29 °C or 22–24 °C, respectively (Fig. 14F). The higher estimate was considered most reasonable, implying a seawater oxygen isotope composition that was consistent with an interglacial world, but not an ice-free one. One possibility for this dichotomy is the apparent disconnect between epeiric seas and open ocean chemistry and temperatures during the Paleozoic (cf. Brand et al., 2009).

Recently, Joachimski et al. (2012) suggested that a warming of about 8 °C occurred during the end of the Permian, starting just before the main extinction event. Seawater temperatures at Meishan and Shangsi varied from 23° to 27 °C in Beds 24d and 24e, and from 25° to 26 °C in Bed 25, and it is not until Bed 27 that temperatures started to exceed 30 °C and reached a maximum of 35 °C in Bed 28 (Joachimski et al., 2012). The slightly elevated temperatures recorded by the conodonts occurred after the mass extinction event placed at the base of Bed 25 by Jin et al. (2000), and therefore could not be the cause for the observed mass extinction. Alternatively, they may be from water depths greater than the 50 m postulated for the Meishan intra-platform depression (Zhang et al., 1996; Joachimski et al., 2012). These results are based on conodonts, which are assumed to be resistant to diagenetic change (Wenzel et al., 2000), but this concept of diagenetic fidelity of conodonts has been seriously challenged by the study of Pucéat et al. (2010). Also, it is further assumed that they incorporated oxygen isotopes into phosphate in equilibrium with their ambient seawater, although, unequivocal overall and individual evidence for these assumptions are lacking (cf. Brand et al., 2004, 2011).

Our Δ_{47} and $\delta^{18}O$ data suggest that actual Late Permian tropical seawater temperatures, up to about 25 cm below the BWF boundary and the mass extinction event, varied, on average, from 34 to 36 °C with occasional lower or higher values (Fig. 14F, Appendix 2). This ~6 °C higher than modern tropical SSTs is probably related to global warming that started with the eruption of the Emeishan flood basalts in South China and other events predating volcanism of the Siberian Trap LIP (e.g., White, 2002; Reichow et al., 2009). A shift to significantly higher temperatures is suggested by the LMC $\delta^{18}O$ values from just below the boundary, generally persisting right into the peak of the extinction event. This same interval witnessed a biodiversity decline from 23 to 3 genera, but the trend reversed just below the Bulla–Tesero boundary (Fig. 14H). This slowing of the biodiversity decline may be related to a drop in the extreme water temperatures of ~39 °C to a 'low' of about 34 °C (Fig. 14F, horizon #VB9C) for this time (Fig. 14H). The sudden global temperature drops may be associated with emission of volcanic sulfate aerosols, characteristic of short-term volcanic winters (Rampino et al., 1988), which can suppress the global warming effect (Pope et al., 1997; Ramanathan et al., 2001). Once the particles settle out of the atmosphere, global temperatures (both air and water), should quickly rebound to their pre-'volcanic winter' levels. This resumption of long-term global warming, concurrent with the biodiversity decline (Fig. 14H), recorded by the biota of the Western Tethys of northern Italy and elsewhere, was in concert with increased volcanism of the Siberian Trap large igneous province (Fig. 14D), and generally oxic sea and ocean surface waters (Fig. 14G).

7.3. Atmospheric constraints of global warming

The atmospheric CO_2 composition of the end-Permian mass extinction has been the subject of much speculation. Emission of volcanic material including CO_2, supplemented by thermogenic CH_4 and sulfate aerosol from the Siberian Trap continental flood basalts reached a climax just before the end-Permian mass extinction event (Reichow et al., 2009), although, this must be recalibrated based on the new ages from the terminal Permian sedimentary successions of South China (Shen et al., 2011a). It has been suggested that atmospheric CO_2 levels were about 3000 ppmv for the Late Permian; prior to the end-Permian mass extinction event (Grard et al., 2005). This is inconsistent with accepted CO_2–global warming effects. Tropical western Tethys sea surface temperatures prior to the event were, on average, about 36 °C (Fig. 14F). This is about 6 °C warmer than modern tropical sea surface temperatures (cf. Palau, Colin, 2002; Brand et al., 2003). Assuming a climate sensitivity of 3 °C per CO_2 doubling (Hansen et al., 2007; Park and Royer, 2011) this would translate into an atmospheric CO_2 concentration of about 1400 ppmv for the Late Permian (though changes, if any, in solar radiation during this time period should be considered). Additional SST warming of a further 4 °C+ during the end–Permian event would be compatible with an atmospheric CO_2 concentration reaching 3000 ppmv.

Our SST estimates for the Late and end of the Permian tropical western Tethys (Fig. 14F) are inconsistent with some models of water

Author's personal copy

temperatures, but are consistent with modeled atmospheric CO_2 concentrations of Kiehl and Shields (2005, their Table 1) and Rampino and Caldeira (2005). For these calculated atmospheric CO_2 levels to be consistent with Siberian Trap flood-basalt CO_2 production of about 11,000 GtC (White and Saunders, 2005), it must have occurred over less than 50,000 years (cf. Rampino et al., 2000; Berner, 2002), which is clearly supported by the proposed rapid shift in the seawater $\delta^{13}C$ curve of about 2000 years (Fig. 14A) leading up to the end-Permian mass extinction.

8. Conclusions

Overall, the end-Permian mass extinction was a biotic catastrophe of global proportions, greater than any extinction observed before or since. We provide high-resolution geochemical information, based on preserved low-Mg calcite brachiopod shells, to gain insight of the events during the Late and the end of the Permian.

1) After evaluation of all available data, we reconstructed high-resolution seawater curves of strontium, carbon, oxygen isotopes (carbonate and seawater), temperature and redox conditions for the Late and end of the Permian.
2) The seawater $\delta^{13}C$ trend suggests a rapid and voluminous discharge of CO_2, just 2000 years before the extinction event, whereas the seawater $\delta^{18}O$ documents drastic changes in tropical SSTs for the 1900 years preceding the event, and the shift in seawater $^{87}Sr/^{86}Sr$ trend at 1500 years defines the onset of continental weathering/erosion likely triggered by acid rain.
3) Our results are consistent with the emission of volcanic CO_2 which may have plunged the Late Permian into a global Greenhouse with average tropical SSTs of about 36 °C.
4) Ce anomaly and authigenic U redox indices indicate that seawater of the western Tethys (and possibly other regions) was oxic to slightly dysoxic in the Late and during the end of the Permian.
5) We suggest that massive release of CO_2, and CH_4 during the 'bulk' Siberian Trap volcanic activity caused a shift from Greenhouse to Hothouse conditions with SSTs rising to more than 39 °C during the end of the Permian and the resulting mass extinction event.
6) Global Hothouse conditions, were possibly briefly interrupted by the emission of sulfate aerosols dropping average SSTs to about 34 °C, and after deposition, Hothouse conditions quickly recovered with continued global warming.
7) Assuming a climate sensitivity of 3 °C per CO_2 doubling, atmospheric CO_2 concentrations were about 1400 ppmv during the Late Permian and increased to about 3000 ppmv for the end of the Permian. We suggest that volcanic emissions of this greenhouse gas with thermogenic methane triggered the end-Permian biotic crisis.

Supplementary data to this article can be found online at http://dx.doi.org/10.1016/j.chemgeo.2012.06.015.

Acknowledgments

We thank M. Lozon, G. Hooper and M. Ouellette (Brock University) for technical assistance. Special thanks to the reviewers for their detailed and helpful comments on the manuscript. We acknowledge NSERC, NSF, Brock University, Memorial University, University of New Hampshire, Yale University, Institute of Biospheric Studies, Università di Ferrara, Università di Milano and Università di Bologna for financial support.

References

Affek, H.P., 2012. Clumped isotope paleothermometry: principles, applications, and challenges. In: Ivany, L.C., Huber, B. (Eds.), Reconstructing Earth's Deep-Time Climate—The State of the Art in 2012: Paleontological Society Papers, 18.

Al-Aasm, I., Veizer, J., 1982. Chemical stabilization of low-Mg calcite: an example of brachiopods. Journal of Sedimentary Petrology 52, 1101–1109.

Algeo, T.J., et al., 2007. Sequencing events across the Permian–Triassic boundary, Guryul Ravine (Kashmir, India). Palaeogeography, Palaeoclimatology, Palaeoecology 252, 328–346.

Algeo, T.J., et al., 2011. Spatial variation in sediment fluxes, redox conditions, and productivity in the Permian–Triassic Panthalassic Ocean. Palaeogeography, Palaeoclimatology, Palaeoecology 308, 65–83.

Assereto, R., Bosellini, A., Fantini Sestini, N., Sweet, W.C., 1973. The Permian–Triassic boundary in the Southern Alps (Italy). Canadian Society Petroleum Geologists, Memoir 2, 176–199.

Attrep, M. Jr, Orth, C.J., Quintana, L.R., 1991. The Permian–Triassic of the Gartnerkofel-1 Core (Carnic Alps, Austria): geochemistry of common and trace elements II: INAA and RNAA. Abhandlungen der Geologischen Bundesanstalt 45, 123–137.

Azmy, K., et al., 2011. Biogenic and abiogenic low-Mg calcite (bLMC and aLMC): evaluation of seawater-REE composition, water masses, and carbonate diagenesis. Chemical Geology 280, 180–190.

Banner, J.L., Hanson, G.N., 1990. Calculation of simultaneous isotopic and trace element variations during water–rock interaction with applications to carbonate diagenesis. Geochimica et Cosmochimica Acta 54, 3123–3137.

Barbin, V., Gaspard, D., 1995. Cathodoluminescence of recent articulated brachiopod shells: implications for growth stages and diagenesis evaluation. Geobios 28, 39–45.

Bau, M., Dulski, P., 1996. Distribution of yttrium and rare-earth elements in the Penge and Kuruman iron-formations, Transvaal Supergroup, South Africa. Precambrian Research 79, 37–55.

Baud, A., Magaritz, M., Holser, W.T., 1989. Permian-Triassic of the Tethys: carbon isotope studies. Geologische Rundschau 78, 649–677.

Benton, M.J., Tverdokhlebov, V.P., Surkov, M.V., 2004. Ecosystem remodelling among vertebrates at the Permian–Triassic boundary in Russia. Nature 432, 97–100.

Berner, R.A., 2002. Examination of hypotheses for the Permo-Triassic boundary extinction by carbon cycle modeling. Proceedings of the National Academy of Sciences 99, 4172–4177.

Berner, R.A., 2005. The carbon and sulfur cycles and atmospheric oxygen from middle Permian to middle Triassic. Geochimica et Cosmochimica Acta 69, 3211–3217.

Birck, L.J., 1986. Precision K–Rb–Sr isotopic analysis: application to Rb–Sr chronology. Chemical Geology 56, 73–83.

Boeckelmann, K., Magaritz, M., 1991. The Permian–Triassic of the Gartnerkofel-1 Core (Carnic Alps, Austria): dolomitization of the Permian–Triassic sequence. Abhandlungen der Geologischen Bundesanstalt 45, 61–68.

Bosellini, A., 1964. Stratigrafia, petrografia e sedimentologia delle Facies carbonatiche al limite permiano-trias nelle Dolomiti occidentali. Museo di Storia Naturale della Venezia Tridentina, Memorie 15, 1–106.

Bowring, S.A., et al., 1998. U/Pb zircon geochronology and tempo of the end-Permian mass extinction. Science 280, 1039–1045.

Brand, U., 2004. Carbon, oxygen and strontium isotopes in Paleozoic carbonate components: an evaluation of original seawater-chemistry proxies. Chemical Geology 204, 23–44.

Brand, U., Veizer, J., 1980. Chemical diagenesis of a multicomponent carbonate system: 1, Trace elements. Journal of Sedimentary Petrology 50, 1219–1236.

Brand, U., Veizer, J., 1981. Chemical diagenesis of a multicomponent carbonate system: 2, Stable isotopes. Journal of Sedimentary Petrology 51, 987–997.

Brand, U., Legrand-Blain, M., Streel, M., 2004. Biochemostratigraphy of the Devonian–Carboniferous boundary global stratotype section and point, Griotte Formation, La Serre, Montagne Noire, France. Palaeogeography, Palaeoclimatology, Palaeoecology 205, 337–357.

Brand, U., Logan, A., Hiller, N., Richardson, J., 2003. Geochemistry of modern brachiopods: applications and implications for oceanography and paleoceanography. Chemical Geology 198, 305–334.

Brand, U., Tazawa, J.-I., Sano, H., Azmy, K., Lee, X., 2009. Is mid-late Paleozoic ocean-chemistry coupled with epeiric seawater isotope records? Geology 37, 823–826.

Brand, U., Azmy, K., Tazawa, J.-I., Sano, H., Buhl, D., 2010. Hydrothermal diagenesis of Paleozoic seamount carbonate components. Chemical Geology 278, 173–185.

Brand, U., et al., 2011. What is the ideal proxy of Paleozoic seawater chemistry? Memoirs of the Association of Australasian Palaeontologists 41, 9–24.

Brand, U., Jiang, G., Azmy, K., Bishop, J.W., Montanez, I.P., 2012a. Diagenetic evaluation of a Pennsylvanian carbonate succession (Bird Spring Formation, Arrow Canyon, Nevada, U.S.A.)—1: Brachiopod and whole rock comparison. Chemical Geology 308–309, 26–39.

Brand, U., et al., 2012b. Oxygen isotopes and Mg content in brachiopod calcite: equilibrium fractionation and a new paleotemperature equation. Goldschmidt Conference, Montreal, Canada, Book of Abstracts.

Brayard, A., et al., 2011. Transient metazoan reefs in the aftermath of the end-Permian mass extinction. Nature Geoscience 4, 693–697.

Broglio Loriga, C., Masetti, D., Neri, C., 1983. La Formazione di Werfen (Scitico) delle Dolomiti occidentali. Rivista Italiana di Paleontologia e Stratigrafia 88, 501–598.

Broglio Loriga, C., Neri, C., Pasini, M., Posenato, R., 1988. Marine fossil assemblages from Upper Permian to lowermost Triassic in the western Dolomites (Italy). In: Cassinis, G. (Ed.), Permian and Permian–Triassic boundary in the South-Alpine segment of the western Tethys, and additional reports: Memorie della Societa Geologica Italiana, 34, pp. 5–44.

Came, R.E., et al., 2007. Coupling of surface temperatures and atmospheric carbon dioxide concentrations during the Palaeozoic Era. Nature 449, 198–201.

Cao, C., Shang, Q.H., 1998. Microstratigraphy of Permo-Triassic transitional sequence of the Meishan section, Zhejiang, China. Palaeoworld 9, 147–152.

Cao, C., Wang, W., Jin, Y.-G., 2002. Carbon isotope excursions across the Permian–Triassic boundary in the Meishan section, Zhejiang Province, China. Chinese Science Bulletin 47, 1125–1129.

Author's personal copy

Cao, C., et al., 2009. Biogeochemical evidence for euxinic oceans and ecological disturbance presaging the end-Permian mass extinction event. Earth and Planetary Science Letters 281, 188–201.

Carpenter, S.J., Lohmann, K.C., 1995. $\delta^{18}O$ and $\delta^{13}C$ values of modern brachiopod shells. Geochimica et Cosmochimica Acta 59, 3749–3764.

Cassinis, G., Perotti, C.R., 2007. A stratigraphic and tectonic review of the Italian Southern Alpine Permian. Palaeoworld 16, 140–172 (Special Issue).

Chen, J., Shao, M., Huo, W., Yu, Y.Y., 1984. Carbon isotope of carbonate strata at Permian–Triassic boundary in Changxing, Zhejiang. Scientia Geologica Sinica 19, 88–93.

Chen, J., Beatty, T.W., Henderson, C.M., Rowe, H., 2009. Conodont biostratigraphy across the Permian–Triassic boundary at the Dawen section, Great Bank of Guizhou, Guizhou Province, South China: implications for the Late Permian extinction and correlation with Meishan. Journal of Asian Earth Sciences 36, 442–458.

Colin, P.L., 2002. Water temperatures on the Palauan Reef Tract: Year 2000. Coral Reef Research Foundation, Koror.

Dennis, K.J., Affek, H., Passey, B.H., Schrag, D.P., Eiler, J.M., 2011. Defining an absolute reference frame for clumped isotope studies of CO_2. Geochimica et Cosmochimica Acta 75, 7117–7131.

Dolenec, T., Lojen, S., Ramovs, A., 2001. The Permian–Triassic boundary in western Slovenia (Idrija Valley section): magnetostratigraphy, stable isotopes, and elemental variations. Chemical Geology 175, 175–190.

Dorritie, D., 2002. Consequences of Siberian Traps volcanism. Science 297, 1808–1809.

Eiler, J.M., 2007. "Clumped-isotope" geochemistry—the study of naturally-occurring multiply-substituted isotopologues. Earth and Planetary Science Letters 262, 309–327.

Eiler, J.M., 2011. Paleoclimate reconstruction using carbonate clumped isotope thermometry. Quaternary Science Reviews 30, 3575–3588.

Erwin, D.H., 1994. The Permo-Triassic extinction. Nature 367, 231–236.

Fairchild, I.J., 1983. Chemical controls of cathodoluminescence of natural dolomites and calcite: new data and review. Sedimentology 30, 579–583.

Farabegoli, E., Viel, G., 1982. Litostratigrafia della Formazione di Werfen (Trias Inf.) delle Dolomiti Occidentali. Industrielle Mineralogia 6, 3–14.

Farabegoli, E., Levanti, D., Perri, M.C., 1986. The Bellerophon Formation in the south-western Carnia, Lavardet-Rioda and Casera Federata Sections, Field conference on Permian and Permian–Triassic boundary in the South alpine segment of the Western Tethys, and additional regional reports. Field guidebook: Italian IGCP project 203, Brescia, pp. 69–75.

Farabegoli, E., Perri, M.C., Posenato, R., 2007. Environmental and biotic changes across the Permian–Triassic boundary in western Tethys: the Bulla parastratotype, Italy. Global and Planetary Change 55, 109–135.

Fio, K., et al., 2010. Stable isotope and trace element stratigraphy across the Permian–Triassic transition: a redefinition of the boundary in the Velebit Mountain, Croatia. Chemical Geology 278, 38–57.

Fritz, P., Smith, D.G.W., 1970. The isotopic composition of secondary dolomites. Geochimica et Cosmochimica Acta 34, 1161–1173.

Goetz, A.J., et al., 2009. Calcite morphology, texture and hardness in the distinct layers of rhynchonelliform brachiopod shells. European Journal of Mineralogy 21, 303–315.

Gorjan, P., Kaiho, K., Chen, Z.-Q., 2008. A carbon-isotopic study of an end-Permian mass-extinction horizon, Bulla, northern Italy: a negative $\delta^{13}C$ shift prior to the marine extinction. Terra Nova 20, 253–258.

Gorjan, P., et al., 2007. Paleoredox, biotic and sulfur-isotopic changes associated with the end-Permian mass extinction in the western Tethys. Chemical Geology 244, 483–492.

Ghosh, P., et al., 2006. $^{13}C-^{18}O$ bonds in carbonate minerals: a new kind of paleothermometer. Geochimica et Cosmochimica Acta 70, 1439–1456.

Grard, A., Francois, L.M., Dessert, C., Dupre, B., Godderis, Y., 2005. Basaltic volcanism and mass extinction at the Permo-Triassic boundary: environmental impact and modeling of the global carbon cycle. Earth and Planetary Science Letters 234, 207–221.

Grasby, S.E., Beauchamp, B., 2009. Latest Permian to Early Triassic basin-to-shelf anoxia in the Sverdrup Basin, Arctic Canada. Chemical Geology 264, 232–246.

Grasby, S.E., Sanei, H., Beauchamp, B., 2011. Catastrophic dispersion of coal fly ash into the oceans during the latest Permian extinction. Nature Geoscience. http://dx.doi.org/10.1038/nge01069 online: 23 January 2011.

Groves, J.R., Rettori, R., Payne, J.L., Boyce, M.D., Altiner, D., 2007. End-Permian mass extinction of Lagenide foraminifers in the Southern Alps (northern Italy). Journal of Paleontology 81, 415–434.

Gruszczynski, M., Halas, S., Hoffman, A., Malkowski, K., 1989. A brachiopod calcite record of the oceanic carbon and oxygen isotope shifts at the Permian/Triassic transition. Nature 337, 64–67.

Gruszczynski, M., Hoffman, A., Malkowski, K., Veizer, J., 1992. Seawater strontium isotopic perturbation at the Permian–Triassic boundary, West Spitsbergen, and its implications for the interpretation of strontium isotopic data. Geology 20, 779–782.

Gruszczynski, M., et al., 1990. Carbon isotopic drop across the Permian–Triassic boundary in SE Sichuan, China. Neues Jahrbuch Geologie und Paläontologie, Monatsheft 10, 600–606.

Hansen, J., et al., 2007. Climate and trace gases. Philosophical Transactions of the Royal Society of London 365, 1925–1954.

Haas, J., et al., 2007. Biotic and environmental changes in the Permian-Triassic boundary interval recorded on a western Tethyan ramp in the Bükk Mountains, Hungary. Global and Planetary Change 55, 136–154.

Heydari, E., Wade, W.J., Hassanzadeh, J., 2001. Diagenetic origin of carbon and oxygen isotope compositions of Permian–Triassic boundary strata. Sedimentary Geology 143, 191–197.

Holser, W.T., et al., 1989. A unique geochemical record at the Permian–Triassic boundary. Nature 337, 39–44.

Horacek, M., Povoden, E., Richoz, S., Brandner, R., 2010. High-resolution carbon isotope changes, litho- and magnetostratigraphy across Permian–Triassic boundary sections in the Dolomites, N.-Italy. New constraints for global correlation. Palaeogeography, Palaeoclimatology, Palaeoecology 290, 58–64.

Huntington, K.W., et al., 2009. Methods and limitations of 'clumped' CO2 isotope ($\Delta47$) analysis by gas-source isotope ratio mass spectrometry. Journal of Mass Spectrometry 44, 1318–1329.

Isozaki, Y., 1997. Permo-Triassic superanoxia and stratified superocean: records from lost deep sea. Science 276, 235–238.

Isozaki, Y., 2009. Integrated 'plume winter' scenario for the double-phased extinction during the Paleozoic–Mesozoic transition: the G-LB and P-TB events from a Panthalassan perspective. Journal of Asian Earth Sciences 36, 459–480.

Jaffres, J.B.D., Shields, G.A., Wallmann, K., 2007. The oxygen isotope evolution of seawater: a critical review of a long-standing controversy and an improved geological water cycle model for the past 3.4 billion years. Earth-Science Reviews 83, 83–122.

Jia, C., et al., 2012. Microbial response to limited nutrients in shallow water immediately after the end-Permian mass extinction. Geobiology 10, 60–71.

Jin, Y.G., et al., 2000. Pattern of marine mass extinction near the Permian–Triassic boundary in South China. Science 289, 432–436.

Joachimski, M.M., et al., 2012. Climate warming in the latest Permian and the Permian–Triassic mass extinction. Geology 40, 195–198.

Jones, B., Manning, D.A.C., 1994. Comparison of geochemical indices used for the interpretation of palaeoredox conditions in ancient mudstones. Chemical Geology 111, 111–129.

Kaiho, K., et al., 2001. End-Permian catastrophe by bolide impact: evidence of a gigantic release of sulfur from the mantle. Geology 29, 815–819.

Kaiho, K., Kajiwara, Y., Chen, Z.-Q., Gorjan, P., 2006. A sulfur isotope event at the end of the Permian. Chemical Geology 235, 33–47.

Kamo, S.L., et al., 2003. Rapid eruption of Siberian flood-volcanic rocks and evidence for coincidence with the Permian–Triassic boundary and mass extinction at 251 Ma. Earth and Planetary Science Letters 214, 75–91.

Kearsey, T., Twitchett, R.J., Price, G.D., Grimes, S.T., 2009. Isotope excursions and paleotemperature estimates from the Permian/Triassic boundary in the Southern Alps (Italy). Palaeogeography, Palaeoclimatology, Palaeoecology 279, 29–40.

Kidder, D.L., Worsley, T.R., 2004. Causes and consequences of extreme Permo-Triassic warming to globally equable climate and relation to the Permo-Triassic extinction and recovery. Palaeogeography, Palaeoclimatology, Palaeoecology 203, 207–237.

Kiehl, J.T., Shields, C.A., 2005. Climate simulation of the latest Permian: implications for mass extinction. Geology 33, 757–760.

Kim, S.-T., O'Neil, J.R., 1997. Equilibrium and nonequilibrium oxygen isotope effects in synthetic carbonates. Geochimica et Cosmochimica Acta 61, 3461–3475.

Klinkhammer, G.P., Palmer, M.R., 1991. Uranium in the oceans: where it goes and why. Geochimica et Cosmochimica Acta 55, 1799–1806.

Knauth, L.P., Kennedy, M.J., 2009. The late Precambrian greening of the Earth. Nature 460, 728–732.

Knoll, A.H., Bambach, R.K., Payne, J.L., Pruss, S., Fischer, W.W., 2007. Paleophysiology and end-Permian mass extinction. Earth and Planetary Science Letters 256, 295–313.

Koeberl, C., Farley, K.A., Peucker-Ehrenbrink, B., Sephton, M.A., 2010. Geochemistry of the end-Permian extinction event in Austria and Italy: no evidence for an extraterrestrial component. Geology 32, 1053–1056.

Korte, C., Kozur, H.W., 2005. Carbon isotope stratigraphy across the Permian/Triassic boundary at Jolfa (NW-Iran), Peitlerkofel (Sas de Putia, Sass de Putia), Pufels (Bula, Bulla), Tesero (all three southern Alps, Italy) and Gerennavar (Bükk Mts., Hungary). Journal of Alpine Geology 47, 119–135.

Korte, C., Kozur, H.W., 2010. Carbon-isotope stratigraphy across the Permian–Triassic boundary: a review. Journal of Asian Earth Sciences 39, 215–235.

Korte, C., Jasper, T., Kozur, H.W., Veizer, J., 2005. $\delta^{18}O$ and $\delta^{13}C$ of Permian brachiopods: a record of seawater evolution and continental glaciation. Palaeogeography, Palaeoclimatology, Palaeoecology 224, 333–351.

Korte, C., Jasper, T., Kozur, H.W., Veizer, J., 2006. $^{87}Sr/^{86}Sr$ record of Permian seawater. Palaeogeography, Palaeoclimatology, Palaeoecology 240, 89–107.

Korte, C., Kozur, H.W., Joachimski, M.M., Strauss, H., Veizer, J., 2004. Carbon, sulfur, oxygen and strontium isotope records, organic geochemistry and biostratigraphy across the Permian/Triassic boundary in Abadeh, Iran. International Journal of Earth Sciences 93, 565–581.

Kozur, H.W., 1998. Some aspects of the Permian–Triassic boundary (PTB) and the possible causes for the biotic crisis around this boundary. Palaeogeography, Palaeoclimatology, Palaeoecology 143, 227–272.

Kozur, H.W., Weems, R.E., 2011. Detailed correlation and age of continental late Changhsingian and earliest Triassic beds: implications for the role of the Siberian Trap in the Permian–Triassic biotic crisis. Palaeogeography, Palaeoclimatology, Palaeoecology 308, 22–40.

Kralik, M., 1991. The Permian–Triassic of the Gartnerkofel-1 core (Carnic Alps, Austria): strontium isotopes and carbonate chemistry. Abhandlungen der Geologischen Bundesanstalt 45, 169–174.

Krull, E.S., et al., 2004. Stable carbon isotope stratigraphy across the Permian–Triassic boundary in shallow marine carbonate platforms, Nanpanjiang Basin, south China. Palaeogeography, Palaeoclimatology, Palaeoecology 204, 297–315.

Labandeira, C.C., Sepkoski Jr., J.J., 1993. Insect diversity in the fossil record. Science 261, 310–315.

Land, L.S., 1980. The isotopic and trace element geochemistry of dolomite: the state of the art. In: Zenger, D.H., Dunham, J.B., Ethington, R.L. (Eds.), Concepts and Models of Dolomitization. SEPM, Oklahoma, pp. 87–110.

Lindholm, R.C., Finkelman, R.B., 1972. Calcite staining: semiquantitative determination of ferrous iron. Journal of Sedimentary Petrology 42, 239–242.

Lhomme, N., Clark, G.K.C., Ritz, C., 2005. Global budget of water isotopes inferred from polar ice sheets. Geophysics Research Letters 32.

Author's personal copy

Magaritz, M., Holser, W.T., 1991. The Permian–Triassic of the Gartnerkofel-1 Core (Carnic Alps, Austria): carbon and oxygen isotope variation. Abhandlungen der Geologischen Bundesanstalt 45, 149–163.

Magaritz, M., Bär, R., Baud, A., Holser, W.T., 1988. The carbon-isotope shift at the Permian/Triassic boundary in the Southern Alps is gradual. Nature 331, 337–339.

Martin, E.E., Macdougall, J.D., 1995. Sr and Nd isotopes at the Permian/Triassic boundary: a record of climate change. Chemical Geology 125, 73–99.

Massari, F., Neri, C., 1997. The infilled of a supradetachment (?) basin: the continental to shallow-marine upper Permian succession in the Dolomites and Carnia (Italy). Sedimentary Geology 110, 181–221.

Massari, F., et al., 1994. Sedimentology, palynostratigraphy and sequence stratigraphy of a continental to shallow- marine rift-related succession: Upper Permian of the Eastern Southern Alps (Italy). Memorie Scienze Geologiche 46, 119–243.

Maxwell, W.D., 1992. Permian and early Triassic extinction of non-marine tetrapods. Palaentology 35, 571–583.

MacDougall, J.D., 1988. Seawater strontium isotopes, acid rain, and the Cretaceous-Tertiary boundary. Science 239, 485–487.

McArthur, J.M., Howarth, R.J., Bailey, T.R., 2001. Strontium isotope stratigraphy: LOWESS version 3: best fit to the marine Sr-isotope curve for 0–509 Ma and accompanying look-up table for deriving numerical age. Journal of Geology 109, 155–170.

Merkel, C., et al., 2009. Mechanical properties of modern calcite- (*Mergelia truncata*) and phosphate-shelled brachiopods (*Discradisca stella* and *Lingula anatina*) determined by nanoindentation. Journal of Structural Biology 168, 396–408.

Mii, H.-S., Grossman, E.L., Yancey, T.E., 1997. Stable carbon and oxygen isotope shifts in Permian seas of West Spitsbergen—global change or diagenetic artifacts. Geology 25, 227–230.

Mu, X., et al., 2009. High-resolution carbon isotope changes in the Permian–Triassic boundary interval, Chongqing, South China: implications for control and growth of earliest Triassic microbialites. Journal of Asian Earth Sciences 36, 434–441.

Musashi, M., Isozaki, Y., Koike, T., Kreulen, R., 2001. Stable carbon isotope signature in mid-Panthalassa shallow-water carbonates across the Permo-Triassic boundary: evidence of 13C depleted superocean. Earth and Planetary Science Letters 191, 9–20.

Muttoni, G., et al., 2009. Opening of the Neo-Tethys Ocean and the Pangea B to Pangea A transformation during the Permian. GeoArabia 14, 17–48.

Newton, R.J., Pecvitt, E.L., Wignall, P.B., Bottrell, S.H., 2004. Large shifts in the isotopic composition of seawater sulphate across the Permo-Triassic boundary in northern Italy. Earth and Planetary Science Letters 218, 331–345.

Nicoll, R.S., Metcalfe, I., Cheng-Yuan, W., 2002. New species of the conodont Genus Hindeodus and the conodont biostratigraphy of the Permian–Triassic boundary interval. Journal of Asian Earth Sciences 20, 609–631.

Park, J., Royer, D.L., 2011. Geologic constraints on the glacial amplification of Phanerozoic climate sensitivity. American Journal of Science 311, 1–26.

Payne, J.L., et al., 2004. Large perturbations of the carbon cycle during recovery from the end-Permian extinction. Science 305, 506–509.

Perri, M.C., Farabegoli, E., 2003. Conodonts across the Permian–Triassic boundary in the Southern Alps. Courier Forschungs-Institute Senckenberg 245, 281–313.

Pope, M.C., Baines, K.H., Ocampo, A.C., Ivanov, B.A., 1997. Energy, volatile production, and climatic effects of the Chicxulub Cretaceous/Tertiary impact. Journal of Geophysical Research 102, 21645–21664.

Popp, B.N., Anderson, T.F., Sandberg, C.A., 1986. Textural, elemental, and isotopic variations among constituents in Middle Devonian limestones, North America. Journal of Sedimentary Petrology 56, 715–727.

Posenato, R., 2001. The athyridoids of the transitional beds between Bellerophon and Werfen formations (uppermost Permian, Southern Alps, Italy). Rivista Italiana di Paleontologia e Stratigrafia 1071, 197–226.

Posenato, R., 2009. Survival patterns of macrobenthic marine assemblages during the end-Permian mass extinction in the western Tethys (Dolomites, Italy). Palaeogeography, Palaeoclimatology, Palaeoecology 280, 150–167.

Posenato, R., 2010. Marine biotic events in the Lopingian succession and latest Permian extinction in the southern Alps (Italy). Geological Journal. http://dx.doi.org/10.1002/gj.1212.

Pucéat, E., et al., 2010. Revised phosphate–water fractionation equation reassessing paleotemperatures derived from biogenic apatite. Earth and Planetary Science Letters 298, 135–142.

Racki, G., Wignall, P.B., 2005. Late Permian double-phased mass extinction and volcanism: an oceanographic perspective. In: Over, D.J., Morrow, J.R., Wignall, P.B. (Eds.), Understanding Late Devonian and Permian–Triassic biotic and climatic events: towards an integrated approach. Elsevier, pp. 263–297.

Ramanathan, V., Crutzen, P.J., Kiehl, J.T., Rosenfeld, D., 2001. Aerosols, climate, and the hydrological cycle. Science 294, 2119–2124.

Rampino, M.R., Self, S., Stothers, R.B., 1988. Volcanic Winters. Annual Review of Earth and Planetary Science 16, 73–99.

Rampino, M.R., Caldeira, K., 2005. Major perturbation of ocean chemistry and a 'Strangelove Ocean' after the end-Permian mass extinction. Terra Nova 17, 554–559.

Rampino, M.R., Projoph, A., Adler, A., 2000. Tempo of the end-Permian event: high resolution cyclostratigraphy at the Permian–Triassic boundary. Geology 28, 643–646.

Rampino, M.R., Projoph, A., Adler, A., Schwindt, D.M., 2002. Abruptness of the end-Permian mass extinction as determined from biostratigraphic and cyclostratigraphic analyses of European western Tethyan sections. Geological Society of America, Special Paper 356, 415–428.

Rantitsch, G., 2007. Robust sequential Factor Analysis of geochemical data from the Permian–Triassic Gartnerkofel-1 core (Southern Alps): the geochemical response to changing paleo-oceanographic conditions in shallow-marine carbonate platforms. Facies 53, 129–140.

Raup, D.M., 1979. Size of the Permo-Triassic bottleneck and its evolutionary implications. Science 206, 217–218.

Reichow, M.K., et al., 2009. The timing and extent of the eruption of the Siberian Traps large igneous province: implications for the end-Permian environmental crisis. Earth and Planetary Science Letters 277, 9–20.

Renne, P.R., Zichao, Z., Richards, M.A., Black, M.T., Basu, A.R., 1995. Synchrony and causal relations between Permian–Triassic boundary crises and Siberian flood volcanism. Science 269, 1413–1416.

Retallack, G.J., 1995. Permian–Triassic life crisis on land. Science 267, 77–80.

Retallack, G.J., 1999. Post-apocalyptic greenhouse paleoclimate revealed by eliest Triassic paleosols in the Sydney Basin, Australia. Geological Society of America Bulletin 111, 52–70.

Retallack, G.J., 2001. A 300-million-year record of atmospheric carbon dioxide from fossil plant cuticles. Nature 411, 287–289.

Retallack, G.J., 2002. Carbon dioxide and climate over the past 300 Myr. Philosophical Transactions of the Royal Society of London 360, 659–673.

Retallack, G.J., 2005. Permian greenhouse crises. In: Lucas, S.G., Ziegler, K.E. (Eds.), The Non-marine Permian: New Mexico Museum of Natural History and Science Bulletin, pp. 256–269.

Retallack, G.J., 2009. Greenhouse crises of the past 300 million years. Geological Society of America Bulletin 121, 1441–1455.

Retallack, G.J., Krull, E.S., 1999. Landscape ecological shift at the Permian–Triassic boundary in Antarctica. Australian Journal of Earth Sciences 46, 785–812.

Retallack, G.J., Jahren, A.H., 2008. Methane release from igneous intrusions of coal during the Late Permian extinction events. Journal of Geology 116, 1–20.

Retallack, G.J., et al., 1998. Search for evidence of impact at the Permian–Triassic boundary in Antarctica and Australia. Geology 26, 979–982.

Retallack, G.J., et al., 2011. Multiple Early Triassic greenhouse crises impeded recovery from Late Permian mass extinction. Palaeogeography, Palaeoclimatology, Palaeoecology 308, 233–251.

Ruban, D., 2010. The Permian/Triassic mass extinction among brachiopods in the Northern Caucasus (northern Palaeo-Tethys): a tentative assessment. Geobios 43, 355–363.

Rubinson, M., Clayton, R.N., 1969. Carbon-13 fractionation between aragonite and calcite. Geochimica et Cosmochimica Acta 33, 997–1002.

Sandberg, P.A., 1983. An oscillating trend in Phanerozoic non-skeletal carbonate mineralogy. Nature 305, 19–22.

Sephton, M.A., et al., 2002. Synchronous record of $\delta^{13}C$ shifts in the oceans and atmosphere at the end of the Permian. In: Koeberl, C., MacLeod, K.G. (Eds.), Catastrophic events and mass extinctions: impacts and beyond. Geological Society of America, Boulder, CO, pp. 455–462.

Sephton, M.A., et al., 2005. Catastrophic soil erosion during the end-Permian biotic crisis. Geology 33, 941–944.

Sepkoski Jr., J.J., 1981. A factor analytical description of the Phanerozoic marine fossil record. Paleobiology 7, 36–53.

Shackleton, N.J., Kennett, J.P., 1975. Paleotemperature history of the Cenozoic and the initiation of Antarctic glaciation: oxygen and carbon isotope analyses in DSDP sites 277, 279, and 281. Initial Report Deep Sea Drilling Project 29, 743–755.

Shen, S., et al., 2010. High-resolution Lopingian (Late Permian) timescale of South China. Geological Journal 45, 122–134.

Shen, S., et al., 2011a. Calibrating the end Permian mass extinction. Science 334, 1367–1372.

Shen, Y., et al., 2011b. Multiple S-isotopic evidence for episodic shoaling of anoxic water during the Late Permian mass extinction. Nature Communication 2 (210). http://dx.doi.org/10.1038/ncomms1217.

Smith, R.M.H., 1995. Changing fluvial environments across the Permian–Triassic boundary in the Karoo Basin, South Africa and possible causes of tetrapod extinctions. Palaeogeography, Palaeoclimatology, Palaeoecology 117, 81–104.

Stanley, S.M., 2006. Influence of seawater chemistry on biomineralization throughout Phanerozoic time: paleontological and experimental evidence. Palaeogeography, Palaeoclimatology, Palaeoecology 232, 214–236.

Stemmerik, L., Bendix-Almgree, S.E., Piasecki, S., 2001. The Permian–Triassic boundary in central East Greenland: past and present views. Bulletin of the Geological Society of Denmark 48, 159–167.

Swart, P.K., Burns, S.J., Leder, J.J., 1991. Fractionation of the stable isotopes of oxygen and carbon in carbon dioxide during the reaction of calcite with phosphoric acid as a function of temperature and technique. Chemical Geology 86, 89–96.

Takahashi, S., Yamakita, S., Suzuki, N., Kaiho, K., Ehiro, M., 2009. High organic carbon content and a decrease in radiolarians at the end of the Permian in a newly discovered continuous section: a coincidence? Palaeogeography, Palaeoclimatology, Palaeoecology 271, 1–12.

Tarutani, T., Clayton, R.N., Mayeda, T.K., 1969. The effect of polymorphism and magnesium substitution on oxygen isotope fractionation between calcium carbonate and water. Geochimica et Cosmochimica Acta 33, 987–996.

Taylor, A.S., Lasaga, A.C., 1999. The role of basalt weathering in the Sr isotope budget of the oceans. Chemical Geology 161, 199–214.

Twitchett, R.J., 2007. The Late Permian mass extinction event and recovery: biological catastrophe in a greenhouse world. In: Sammonds, P.R., Thompson, J.M.T. (Eds.), Advances in Earth Science from Earthquake to Global Warming. Imperial College Press, London, pp. 69–90.

Twitchett, R.J., Looy, C.V., Morante, R., Visscher, H., Wignall, P.B., 2001. Rapid and synchronous collapse of marine and terrestrial ecosystems during the end-Permian biotic crisis. Geology 29, 351–354.

Veizer, J., 1983. Trace elements and stable isotopes in sedimentary carbonates. In: Reeder, R.J. (Ed.), Carbonates: Mineralogy and Chemistry. Mineralogical Society of America, Blacksburg, pp. 265–299.

Veizer, J., 1989. Strontium isotopes in seawater through time. Annals Review Earth Planetary Sciences 17, 141–167.

Author's personal copy

Wallmann, K., 2001. The geological water cycle and the evolution of marine ^{18}O values. Geochimica et Cosmochimica Acta 65, 2469–2485.
Wang, W., et al., 2007. Isotopic chemostratigraphy of the microbialite-bearing Permian–Triassic boundary section in the Zagros Mountains, Iran. Chemical Geology 244, 708–714.
Ward, P.D., et al., 2005. Abrupt and gradual extinction among Late Permian vertebrates in the Karoo Basin, South Africa. Science 307, 709–714.
Wenzel, B., Lécuyer, C., Joachimski, M.M., 2000. Comparing oxygen isotope records of Silurian calcite and phosphate—^{18}O compositions of brachiopods and conodonts. Geochimica et Cosmochimica Acta 64, 1859–1872.
Wignall, P.B., 2007. The End-Permian mass extinction—how bad did it get? Geobiology 5, 303–309.
Wignall, P.B., Hallam, A., 1992. Anoxia as a cause of the Permian/Triassic extinction: facies evidence from northern Italy and the western United States. Palaeogeography, Palaeoclimatology, Palaeoecology 93, 21–46.
Wignall, P.B., Twitchett, R.J., 1996. Oceanic anoxia and the End Permian mass extinction. Science 272, 1155–1158.
Wignall, P.B., Twitchett, R.J., 2002. Extent, duration and nature of the Permian-Triassic superanoxic event. In: McCleod, K.C. (Ed.), Catastrophic events and mass extinctions: impacts and beyond. Geological Society of America. Special Paper 356, 395–413.
Wignall, P.B., Newton, R.J., Brookfield, M.E., 2005. Pyrite framboid evidence for oxygen-poor deposition during the Permian–Triassic crisis in Kashmir. Palaeogeography, Palaeoclimatology, Palaeoecology 216, 183–188.
White, R.V., 2002. Earth's biggest 'whodunnit': unravelling the clues in the case of the end-Permian mass extinction. Philosophical Transactions of the Royal Society of London 360, 2963–2985.
White, R.V., Saunders, A.D., 2005. Volcanism, impact and mass extinctions: incredible or credible coincidences? Lithos 79, 299–316.
Xu, D.-Y., Yan, Z., 1993. Carbon isotope and iridium event markers near the Permian/Triassic boundary in the Meishan section, Zhejiang Province, China. Palaeogeography, Palaeoclimatology, Palaeoecology 104, 171–176.
Yin, H., Zhang, K., Tong, J., Yang, Z., Wu, S., 2001. The global stratotype section and point (GSSP) of the Permian–Triassic boundary. Episodes 24, 102–114.
Zaarur, S., Olack, G., Affek, H., 2011. Paleo-environmental implication of clumped isotopes in land snail shells. Geochimica et Cosmochimica Acta 75, 6859–6869.
Zhang, K.X., Tong, J.N., Yin, H.F., Wu, S.B., 1996. Sequence stratigraphy near the Permian–Triassic boundary at Meishan section, South China. In: Yin, H.F. (Ed.), The Paleozoic–Mesozoic boundary, candidates of the Global Stratotype Section and Point of the Permian–Triassic boundary. China University of Geosciences Press, Wuhun, pp. 72–83.
Zhang, R., Follows, M.J., Grotzinger, J.P., Marshall, J.D., 2001. Could the Late Permian deep ocean have been anoxic? Paleoceanography 16, 317–329.
Zhou, L., Kyte, F.T., 1988. The Permian–Triassic boundary events: a geochemical study of three Chinese sections. Earth and Planetary Science Letters 90, 411–421.